Fall 2009

Active vibration control of a flexible beam.

Shawn Le
San Jose State University

ACTIVE VIBRATION CONTROL OF A FLEXIBLE BEAM

A Thesis

Presented To

The Faculty of the Department of Mechanical and Aerospace Engineering

San José State University

In Partial Fulfillment

of the Requirement for the Degree

Master of Science

by

Shawn Le

December 2009

SAN JOSÉ STATE UNIVERSITY

The Undersigned Thesis Committee Approves the Thesis Titled

ACTIVE VIBRATION CONTROL OF A FLEXIBLE BEAM

by
Shawn Thanhson Le

APPROVED FOR THE DEPARMENT OF
MECHANICAL AND AEROSPACE ENGINEERING

Dr. Ji Wang,	Department of Mechanical and Aerospace Engineering	10/05/09 Date
Dr. Neyram Hemati,	Department of Mechanical and Aerospace Engineering	10/13/09 Date
Dr. Winncy Du,	Department of Mechanical and Aerospace Engineering	10/08/09 Date

APPROVED FOR THE UNIVERSITY

Associate Dean,	Office of Graduate Studies and Research	2/5/10 Date

ABSTRACT

ACTIVE VIBRATION CONTROL OF A FLEXIBLE BEAM

by Shawn Le

There has been tremendous growth in the study of vibration suppression of smart material structures with lead zironate titanate (PZT) material by the control engineering community. This thesis considers a cantilever beam with bonded piezoceramic actuators and a sensor for the study of vibration control. The flexible beam dynamic model is first derived analytically according to the Euler Bernoulli Beam Theory. The first three mode shapes and natural frequencies of the beam are constructed analytically and verified with finite element analysis. The validity of the smart structure was experimentally verified. The natural frequencies and damping parameters for each mode were experimentally verified and adjusted. In this study, a transfer function consisting of the first three modes is constructed to implement both classical derivative (D) and proportional and derivative (PD) control. Then a state space model consisting of the first two modes of the beam is constructed to design and implement the modern linear quadratic regulator (LQR) state feedback control algorithm. A smart-structure beam station was built according to the instruction of Steven Griffin [6]. The Griffin's analog circuit was modified to integrate with the Matlab-Quanser real-time control unit. In the analytical and experimental study, the D, PD, and LQR state-feedback controller provided significant vibration suppression.

ACKNOWLEDGEMENTS

First and foremost I would like to thank my committee chair and advisor, Professor Ji Wang, for his guidance and support for making this work possible. I would like to thank Professor Winncy Du and Professor Neyram Hemati for taking the time and interest in serving as my committee members. I would like to thank my two close electrical engineering friends from San Diego, Khang Nguyen and Lam Tran. They have been great in helping me understand the electrical circuit of this work. I would especially like to thank my friend and classmate Howlit Ch'ng for keeping me company while working on this thesis in the San Jose State University Control Lab. In addition, I would like to thank him for helping me set up and use the Matlab-Quanser real-time control system.

TABLE OF CONTENTS

LIST OF FIGURES viii

LIST OF TABLES xi

1. Introduction 1

2. Modeling of the Beam 2

2.2 Piezoceramic Actuator Model 6

2.3 Piezoceramic Sensor Model 8

2.4 Derivation of the Transfer Function with Actuator 9

2.5 Derivation of the Transfer Function with Actuator-Sensor 10

2.6 Mode Shapes of the Beam 12

2.7 Impulse Response and Bode Plot of the Transfer Function 14

2.8 Parameters of the Piezoceramic Laminate Beam 17

3. Experimental Setup 18

3.1 Real-Time Experimental Setup with Simulink and Quanser 20

3.1.1 Real-Time Hardware Setup 21

3.2 Experimental Identification 24

4. Vibration Control Method 27

4.1 Method 1: Derivative Control 28

4.2 Method 2: Proportional and Derivative Control, PD Controller 29

4.2.1 PD Controller Simulation 30

4.2.2 PD Real-Time Control 33

4.3 Method 3: LQR State Feedback with Observer Design- LQR Controller 35

4.3.1 State Space Dynamic Model Derivation 35

4.3.2 Observability and Controllabilty 36

4.3.3 Observer Design 38

4.3.4 LQR State Feedback Gain 39

4.3.5 LQR State Feedback Controller Simulation 39

4.3.6 LQR Real-Time Control 47

5. Results and Discussion 52

6. Conclusion and Recommendations 54

BIBLIOGRAPHY 56

Appendix A Mathcad Analysis 57

Appendix B Matlab M Files 72

LIST OF FIGURES

Figure 1. Cantilever Beam with Bonded PZT Actuators and Sensor. 3

Figure 2. Bending Moment of Actuator..... 6

Figure 3. Charge Amplifier and PZT Sensor. 8

Figure 4. Mode Shape of Beam Derived Theoretically. 12

Figure 5. Mode 1 and Mode 2 Respectively with Pro-Mechanica. 13

Figure 6. Mode 3 of the Beam with Pro-Mechanica..... 13

Figure 7. Impulse Reponse of Beam Deflection at the Tip of the Beam Simulated in Simulink..... 15

Figure 8. Bode Plot of the Transfer Function of Equation (20)..... 16

Figure 9. The Impulse Response of the Voltage Sense by the Piezoceramic Material. ... 16

Figure 10. Bode Plot of the Transfer Function Equation (27). 17

Figure 11. Beam Circuit Detail of LM324 Operational Amplifier. 19

Figure 12. Beam Circuit Interfacing to Quanser between Griffin's Analog Circuit with the Maltab-Quanser System. 20

Figure 13. Experimental Beam Station Connected to Simulink-Quanser. 21

Figure 14. View of Beam Station and Circuit..... 22

Figure 15. Close Up Top View of Beam Station Showing Piezoceramic Actuator and Sensor..... 22

Figure 16. Close Up Bottom View of Beam Station Showing Piezoceramic Actuator ... 23

Figure 17. Quanser DAQ Board with Analog. 23

Figure 18. Real-Time Implementation of Open Loop Actuation at the Beam Natural Frequency..... 25
Figure 19. Plot of Open Loop Actuation at Resonant Frequency of 97.5 rad/s..... 26
Figure 20. Open Loop Reponse of Beam Deflected at Approximately 1 inch..... 26
Figure 21. Plot to Calculate Damping Coefficient of First Mode Open Loop Response. 27
Figure 22. Derivative Controller of *Make* Analog Circuit..... 29
Figure 23. Simulink Open Loop Response Simulation of Transfer Function for First Three Modes. 30
Figure 24. Plot of Simulink Open Loop Response Simulation..... 30
Figure 25. PD Controller Simulation of Beam Vibration Suppression. 31
Figure 26. PD Vibration Suppression Simulation, P=40, D=1.5..... 32
Figure 27. PD Vibration Suppression Simulation, P=17, D=0.01..... 32
Figure 28. Real-Time PD Controller Implementation Block Diagram Simulink..... 33
Figure 29. Real-Time Plot of PD Vibration Suppression, P=17, D=0.01..... 34
Figure 30. Real-Time Plot of Control Voltage. 34
Figure 31. State Space Open Loop Response with Initial Condition. 40
Figure 32. Plot of State Space Open Loop Response with Initial Condition..... 40
Figure 33. State Space with Observer and LQR State Feedback..... 41
Figure 34. Voltage Sense of LQR Controller at $\alpha=1$, $\beta=1$..... 42
Figure 35. LQR Control Voltage at $\alpha=1$, $\beta=1$..... 42
Figure 36. Voltage Sense of LQR Controller at $\alpha=10$, $\beta=1$..... 43
Figure 37. LQR Control Voltage at $\alpha=10$, $\beta=1$..... 43

Figure 38. Voltage Sense of LQR Controller at α=100, β=1. 44

Figure 39. LQR Control Voltage at α=100, β=1 44

Figure 40. Voltage Sense of LQR Controller at α=1, β=0.001. 45

Figure 41. LQR Control Voltage at α=1, β=0.001 45

Figure 42. Voltage Sense of LQR Controller at α=1, β=0.005. 46

Figure 43. Real-Time Control of LQR Controller with Observer and State Feedback in Simulink. 48

Figure 44. Real-Time Voltage Sense Plot of LQR Control at α=1, β=1 49

Figure 45. Real-Time Voltage Sense Plot of LQR Control at α=10, β=1 49

Figure 46. Real-Time Control Voltage of LQR Controller at α=10, β=1. 50

Figure 47. Real-Time Voltage Sense Plot LQR Control at α=100, β=1. 50

Figure 48. Real-Time Control Voltage of LQR Controller at α=100, β=1. This data shows the control voltage before the ±36V limitation of the hardware. 51

LIST OF TABLES

Table 1. Constant Values for λ. 5

Table 2. Comparison of the 3 Mode Shape Between Pro-Mechanica and Theoretical Method. 14

Table 3. Parameters of Aluminum 6064 Beam. 17

Table 4. Parameters of PZT PSI-4A4E. 18

Table 5. Comparison Controller Performance Based on Settling Time. 53

1. Introduction

The interest of this study is active vibration damping in a flexible structure bonded with piezoelectric materials such as piezoelectric ceramic material (PZT). Piezoceramic layers bonded to the surface of or into a manufactured flexible structure member can act as either control actuator or sensor [6]. The piezoelectric effect consists of the ability to strain when the crystalline material is exposed to voltage. Oppositely, it produces electrical charge when strained [1]. A flexible structure with the piezoelectric elements bonded on it becomes what is called a smart structure. Application of smart structures range from K2 skis to space structures, where minimal vibration is highly desirable [6]. This smart material technology may be applied to the construction of high-rise buildings to counter the devastating effects of vibration from an earthquake [4].

In this study, a cantilever beam with the smart material (PZT) bonded on it was modeled with the Euler Bernoulli Beam theory [6]. With the model derived, different controllers could be designed and simulated in Simulink and implemented in real-time to study the improvement of the dampening effect on the beam.

2. Modeling of the Beam

A flexible aluminum cantilever beam with a pair of PZT actuators and a single PZT sensor was modeled with the Euler-Bernoulli Beam theory. There was a derivation of the transfer function of the system relating the elastic deflection of the beam to a voltage applied to the piezoceramic actuator [1]. There was also a derivation of the transfer function of the relationship between the voltage applied to the actuator and the voltage induced in the piezoceramic sensor. The transfer function derived was verified by comparing the first three mode shapes and natural frequencies of the beam to the finite element analysis result in Pro-Mechanica [1].

2.1 Derivation of the Flexible Beam Mode Shape

A piezoceramic laminate cantilevered beam is illustrated in Figure 1. The beam is fixed at one end and free at the other end. Two piezoceramic actuators patches and one piezoceramic sensor (PZT) are used as shown in Figure 1. The parameters in Figure 1 are given in Table 4 . The Euler Bernoulli Beam theory gives the partial differential beam equation in Equation (1) [1, 8].

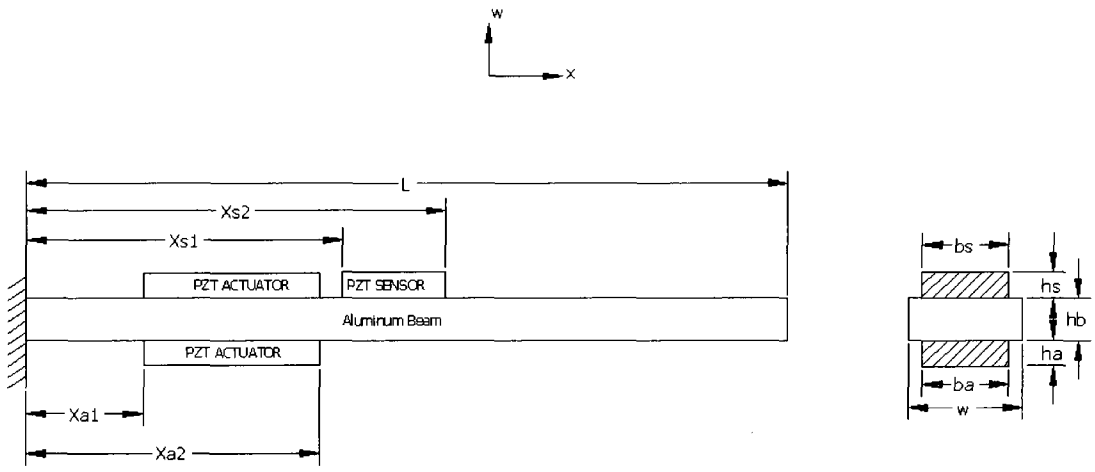

Figure 1. Cantilever Beam with Bonded PZT Actuators and Sensor.

The partial differential equation describing the dynamic of the flexible beam without damping force is:

$$\rho_b A_b \frac{\partial^2 w}{\partial^2 t} + E_b I_b \frac{\partial^4 w}{\partial^4 x} = M_a \frac{\partial^2 R(x)}{\partial x^2} \tag{1}$$

where:

ρ_b = mass density of material of beam

A_b = cross sectional area of beam

E_b = Young's Modulus of beam

I_b = first moment of inertia, $I_b = \frac{b_a h_b^3}{3}$ of beam

h_b = thickness of beam

b_a = width of beam

w = beam transverse displacement

M_a = bending moment acting on beam.

where R is the generalized location function

$$R(x) = H(x - x_{a1}) - H(x - x_{a2}) \tag{2}$$

and H is the Heaviside function. x_{a1} and x_{a2} are locations of the actuators [8].

The transverse displacement is expressed in terms of infinite series

$$w(x,t) = \sum_{i=1}^{\infty} \phi_i(x)\eta_i(t) \tag{3}$$

where $\phi_i(x)$ is the i^{th} mode shape for the cantilever beam and $\eta_i(t)$ is the corresponding generalized displacement. The homogeneous solution to the partial differential Equation (1) is

$$F_h(x) = A\cos\beta x + B\sin\beta x + C\cosh\beta x + D\sinh\beta x \tag{4}$$

For a clamp-free cantilever beam, the boundary conditions are:

$$w(0,t) = 0 \tag{4a}$$

$$\frac{\partial w(0,t)}{\partial x} = 0 \tag{4b}$$

$$\frac{\partial^2 w(l,t)}{\partial x^2} = 0 \tag{4c}$$

$$\frac{\partial w^3(l,t)}{\partial x^3} = 0 \tag{4d}$$

where l is the length of the beam. The boundary conditions applied to Equation (4) give the following 4 equations:

$$A + C = 0 \tag{5}$$

$$B + D = 0 \tag{5a}$$

$$-A\cos\beta l - B\sin\beta l + C\cosh\beta l + D\sinh\beta l = 0 \tag{5b}$$

$$A\cos\beta l - B\sin\beta l + C\cosh\beta l + D\sinh\beta l = 0 \tag{5c}$$

The substitution of the first three equations into the last equation results in

$$A\left[1 + \frac{(\cos\beta l + \cosh\beta l)^2}{(\sin^2\beta l + \sinh^2\beta l)}\right] = 0 \tag{6}$$

To satisfy the boundary conditions, A=0 is to a trivial solution and B = C = D = 0.

This result to

$$\left[\frac{(\cos\beta l + \cosh\beta l)^2}{(\sin^2\beta l + \sinh^2\beta l)}\right] = -1 \tag{7}$$

This equation is reduced to

$$(\cos\beta l \cosh\beta l) = -1 \tag{7a}$$

The equation is solved with an infinite number constant of $\beta_i l$'s. The first three values are given in Table 1. Note that ($\beta_i l = \lambda_i$).

Table 1. Constant Values for λ.

i	$\lambda = \beta_i l$
1	1.875104069
2	4.694091133
3	7.85475743

The mode shape, $\phi_i(x)$ is

$$\phi_i(x) = C_i\left[\cos\left(\frac{\lambda_i x}{l}\right) - \cosh\left(\frac{\lambda_i x}{l}\right) - \frac{\cos\left(\frac{\lambda_i x}{l}\right) + \cosh\left(\frac{\lambda_i x}{l}\right)}{\sin\left(\frac{\lambda_i x}{l}\right) + \sinh\left(\frac{\lambda_i x}{l}\right)} \cdot \left(\sin\left(\frac{\lambda_i x}{l}\right) - \sinh\left(\frac{\lambda_i x}{l}\right)\right)\right] \tag{8}$$

where the constant, C_i, can be determined from the orthogonality expression:

$$\int_0^l \phi_i^2(x)dx = 1 \tag{9}$$

and

$$\int_0^l \phi_i \phi_j dx = 0 \quad \text{if} \quad i \neq j \tag{9a}$$

2.2 Piezoceramic Actuator Model

Two PZT patches are laminated to the top and the bottom of the beam structure with epoxy glue as shown in Figure 2. The PZT patches have an actuating capability, which is governed by the piezoelectric constant (d_{31}).

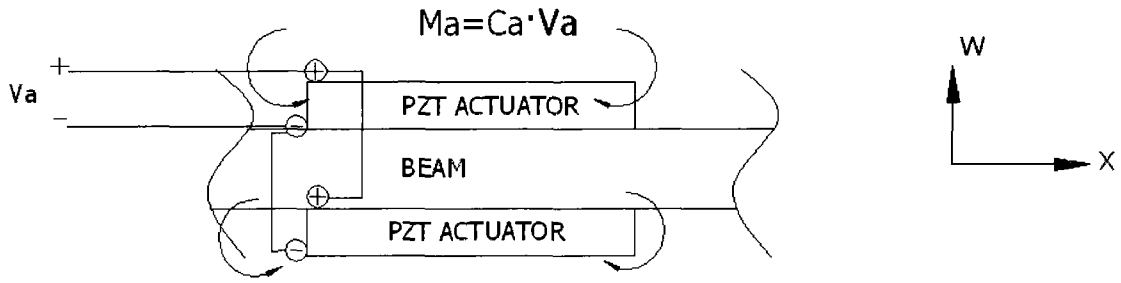

Figure 2. Bending Moment of Actuator.

The 3 in the d_{31} implies that the charge is collected on the polarized surfaces or along the w-axis as shown in Figure 1, and the 1 implies that the force is generated along the longitudinal x-axis. When a voltage (V_a) is applied in the same direction as the polarization of the piezoceramic electric material, the material is elongated along the x-axis. The bending moment (M_a) is shown in Figure 2 [2]. When an opposite V_a is applied to the polarized direction, the material is contracted along the x-axis [2]. The moment induced by the voltage is given in the form of

$$M_a(t) = C_a V_a(t) \tag{10}$$

where the constant, C_a, is given as

$$C_a = \left(\frac{1}{2} E_a d_{31} b_a (h_b + h_a) \right) \tag{10a}$$

where

E_a = Young's modulus of the piezoceramic actuator

d_{31} = electric charge constant (isotropic plane)

b_a = width of the actuator

h_b = thickness of the beam

h_a = thickness of the actuator

The total distributed load, $q_a(x,t)$, in Equation 1 is given in the form of

$$M_a \frac{\partial^2 R(x)}{\partial x^2} = q_a(x,t) \tag{11}$$

2.3 Piezoceramic Sensor Model

A PZT sensor is laminated on the top surface of the beam as shown in Figure 3. It also shows the PZT sensor connected to a charge amplifier.

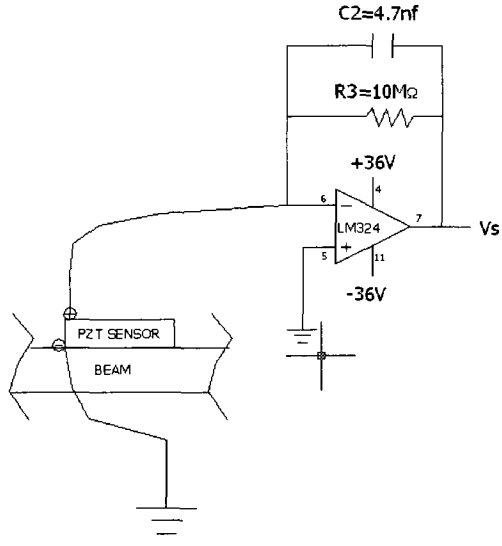

Figure 3. Charge Amplifier and PZT Sensor.

The structural deformation of the beam induces strain to the laminar sensor. The electric charge of the piezoceramic sensor ($Q_s(t)$) is equal to the integral of the electric charge distribution over the entire length of the piezoceramic materials multiplied by the sensor width (b_s) [1]. The electric charge distribution ($q(x,t)$) is given as

$$q(x,t) = \left(\frac{k_{31}^2}{g_{31}}\right)\varepsilon_c(x,t) \tag{11a}$$

where k_{31} is the coupling coefficient, g_{31} denotes the piezoelectric voltage coefficient, and $\varepsilon_c(x,t)$ is the strain in the sensor patch. The strain ($\varepsilon_c(x,t)$) is related to the curvature of the beam in the form of

$$\varepsilon_c(x,t) = -\left(\frac{t_b}{2} + t_a\right)\frac{\partial^2 w}{\partial x^2} \tag{12}$$

The total charge accumulated on the sensing layer can by found by integrating $q(x,t)$ over the entire area of the piezoelectric sensing element.

$$Q_s(t) = -b_s \int_{x_{s1}}^{x_{s2}} q(x,t)dx = -b_s\left(\frac{t_b}{2} + t_a\right)\left(\frac{k_{31}^2}{g_{31}}\right)\frac{\partial^2 w(x,t)}{\partial x^2}\Bigg|_{x_{s1}}^{x_{s2}} \tag{13}$$

2.4 Derivation of the Transfer Function with Actuator

From [1], the substitution of the Equation (2) into (1) results to Equation (14).

$$\sum_{i=1}^{\infty}\left[\rho_b A_b \phi_i(x)\ddot{\eta}_i(t) + E_b I_b \phi_i''''(x)\eta_i(t)\right] = M_a(t)\frac{\partial^2 R(x)}{\partial x^2} \tag{14}$$

Because $\int_0^l \phi_i^2(x)dx = 1$, Equation (14) is integrated by $\int_0^l \phi_i(x)dx$ to yield

$$\left(\rho_b A_b \int_0^l \phi_i^2(x)dx\right)\ddot{\eta}_i(t) + \left(E_b I_b \int_0^l \phi_i^2(x)\phi_i''''(x)dx\right)\eta_i(t) = M_a(t)\int_0^l \frac{\partial^2 R(x)}{\partial x^2}\phi_i(x)dx \tag{15}$$

where

$$\phi_i''''(x) = \lambda_i^4 \phi_i(x) \tag{15a}$$

Equation (15) becomes

$$\left(\rho_b A_b\right)\ddot{\eta}_i(t) + E_b I_b \lambda_i^4 \eta_i(t) = M_a(t)\int_0^l \frac{\partial^2 R(x)}{\partial x^2}\phi_i(x)dx \tag{15b}$$

which simplifies Equation (15) to the second order Equation (1)

$$\ddot{\eta}_i(t)+\omega_{ni}^2\eta_i(t)=k_a\left[\phi_i'(x_{a2})-\phi_i'(x_{a1})\right]V_a(t) \qquad i=1,2,3... \tag{16}$$

where

$$\omega_{ni}^2=\frac{E_bI_b}{\rho_bA_b}\lambda_i^4 \tag{17}$$

$$k_a=\frac{\left(\frac{1}{2}E_ad_{31}b_a(h_b+h_a)\right)}{\rho_aA_a} \tag{18}$$

To include damping, ζ_i, the Equation (16) becomes

$$\ddot{\eta}_i(t)+2\zeta_i\omega_{ni}\dot{\eta}_i(t)+\omega_{ni}^2\eta_i(t)=k_a\left[\phi_i'(x_{a2})-\phi_i'(x_{a1})\right]V_a \tag{19}$$

Take Laplace transformation of Equation (19) and substitute into Equation (3) yields

$$\frac{w(x,s)}{V_a(s)}=\sum_{i=1}^{\infty}\frac{k_a\phi_i(x)\left[\phi_i'(x_{a2})-\phi_i'(x_{a1})\right]}{s^2+2\zeta_i\omega_{ni}s+\omega_{ni}^2} \tag{20}$$

2.5 Derivation of the Transfer Function with Actuator-Sensor

The total charge of the sensor in Equation (13)

$$Q_s(t)=-b_s\int_{x_{s1}}^{x_{s2}}q(x,t)dx=-b_s\left(\frac{t_b}{2}+t_a\right)\left(\frac{k_{31}^2}{g_{31}}\right)\left.\frac{\partial^2w(x,t)}{\partial x^2}\right|_{x_{s1}}^{x_{s2}}$$

evaluated at the position of the sensor, x_{s2} and x_{s1} give

$$\left.\frac{\partial^2w(x,t)}{\partial x^2}\right|_{x_{s1}}^{x_{s2}}=\sum_{i=1}^{\infty}\eta_i(t)[\phi_i(x_{s2})-\phi_i(x_{s1})] \tag{21}$$

results to

$$Q_s(t) = k_s \sum_{i=1}^{\infty} \eta_i(t)[\phi_i'(x_{s2}) - \phi_i'(x_{s1})] \tag{22}$$

where

$$k_s = -b_s\left(\frac{t_b}{2} + t_a\right)\left(\frac{k_{31}^2}{g_{31}}\right) \tag{23}$$

The relationship between the voltage, $V_s(t)$, and the total charge, $Q(t)$, is given [1] as

$$V_s(t) = \frac{Q_s(t)}{C_s b_s\left(x_{s2} - x_{s1}\right)} \tag{24}$$

where

C_s is the capacitance per unit area of the piezoelectric sensor

$b_s\left(x_{s2} - x_{s1}\right)$ is the surface area of the piezoelectric sensor

Substituting $Q_s(t)$ into $V_s(t)$ yields:

$$V_s(t) = \frac{k_s \sum_{i=1}^{\infty} \eta_i(t)[\phi_i'(x_{s2}) - \phi_i'(x_{s1})]}{C_s b_s\left(x_{s2} - x_{s1}\right)} \tag{25}$$

From Equation (19)

$$\eta_i(t) = \frac{k_a\left[\phi_i'(x_{a2}) - \phi_i'(x_{a1})\right]}{\left(s^2 + 2\zeta_i\omega_{ni}s + \omega_{ni}^2\right)} V_a(t) \tag{26}$$

Substitute Equation (26) into Equation (25) yield Equation (27), the transfer function relating the input voltage of the actuator to the voltage induced by the piezoelectric sensor.

$$\frac{V_s(s)}{V_a(s)} = \sum_{i=1}^{\infty} \frac{k_s k_a \left[\phi_i'(x_{s2}) - \phi_i'(x_{s1})\right]\left[\phi_i'(x_{a2}) - \phi_i'(x_{a1})\right]}{C_s b_s \left(x_{s2} - x_{s1}\right)\left(s^2 + 2\zeta_i \omega_{ni} s + \omega_{ni}^2\right)} \tag{27}$$

2.6 Mode Shapes of the Beam

The first 3 bending mode shapes were plotted from Equation (8) as shown in Figure 4 and verified with Pro-Mechanica finite element analysis as shown in Figure 5 and Figure 6. The analytical mode shapes analysis agrees well with the finite element analysis. Table 1 shows a comparison of the 3 natural frequencies of the first 3 modes of the beam. The analytical natural frequencies of the cantilever beam are obtained from Equation (17). The natural frequencies of both methods are very close to one another.

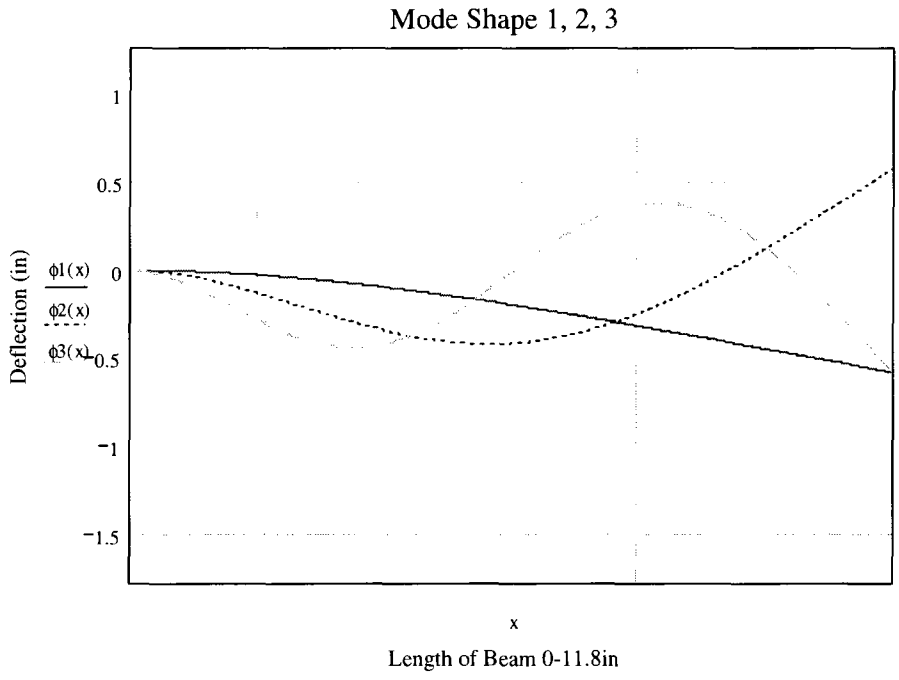

Figure 4. Mode Shape of Beam Derived Theoretically.

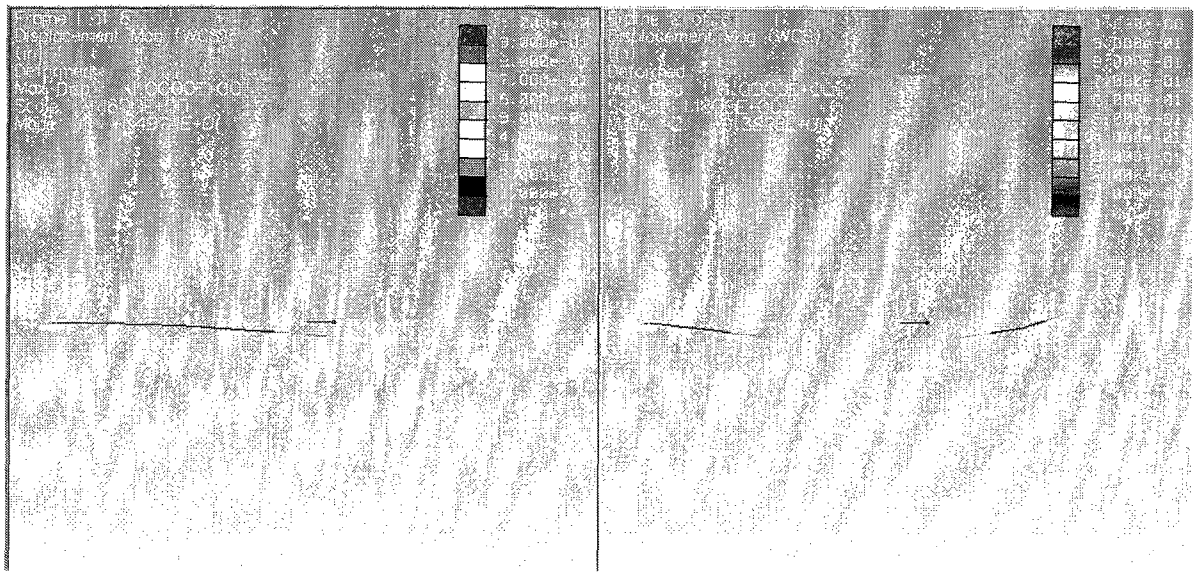

Figure 5. Mode 1 and Mode 2 Respectively with Pro-Mechanica.

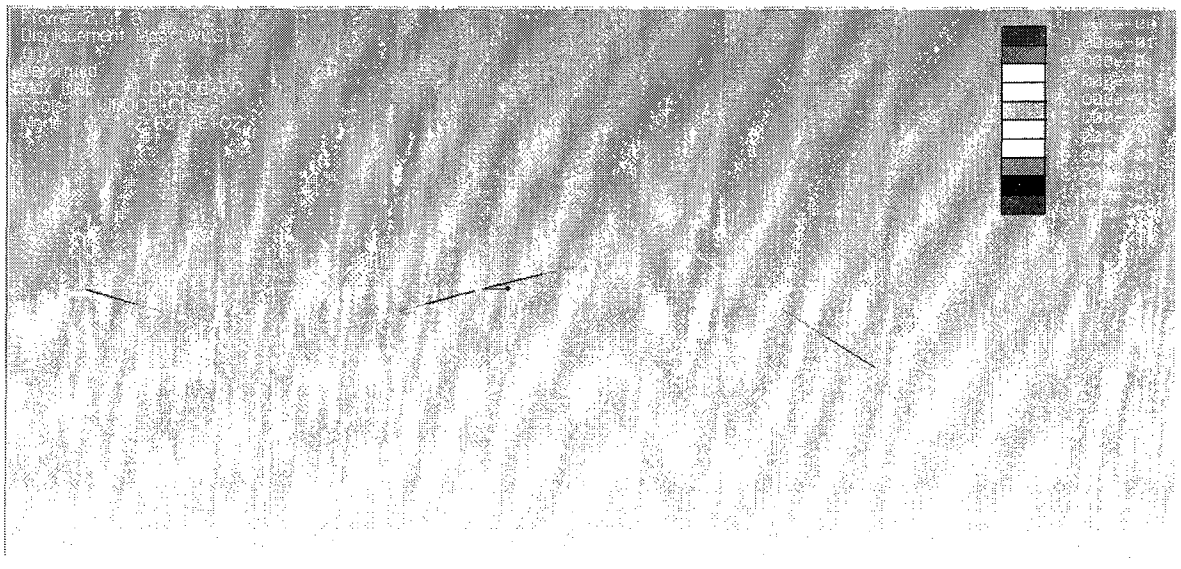

Figure 6. Mode 3 of the Beam with Pro-Mechanica.

Table 2. Comparison of the 3 Mode Shape Between Pro-Mechanica and Theoretical Method.

	Model (rad/s)	Mode 2 (rad/s)	Mode 3 (rad/s)
Pro-Mechanica	95.3618	597.5569	1714
Theoretical (Euler Bernoulli)	92.677	580.79	1626

2.7 Impulse Response and Bode Plot of the Transfer Function

The impulse response for two cases was simulated in Simulink per Equation (20) and (27). The impulse response of the first case is a tip deflection ($x = l$) of the beam and is shown in Figure 7. The second case is the impulse response of the sensor voltage and is shown in Figure 9. The Bode plots of the two cases are shown in Figure 8 and Figure 10. Both Bode plots show the resonant peaks to be at the same location. The damping coefficient is assumed to be $\zeta_{1,2,3} = 0.01$.

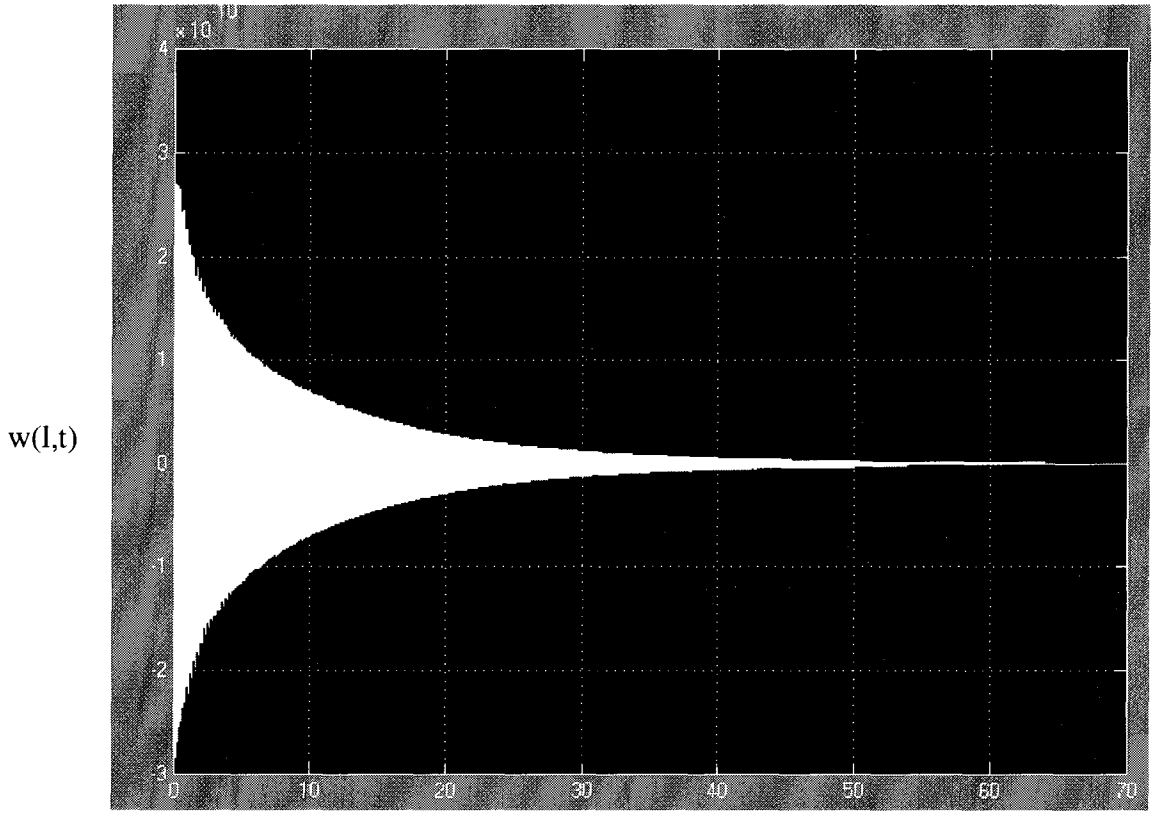

Figure 7. Impulse Reponse of Beam Deflection at the Tip of the Beam Simulated in Simulink.

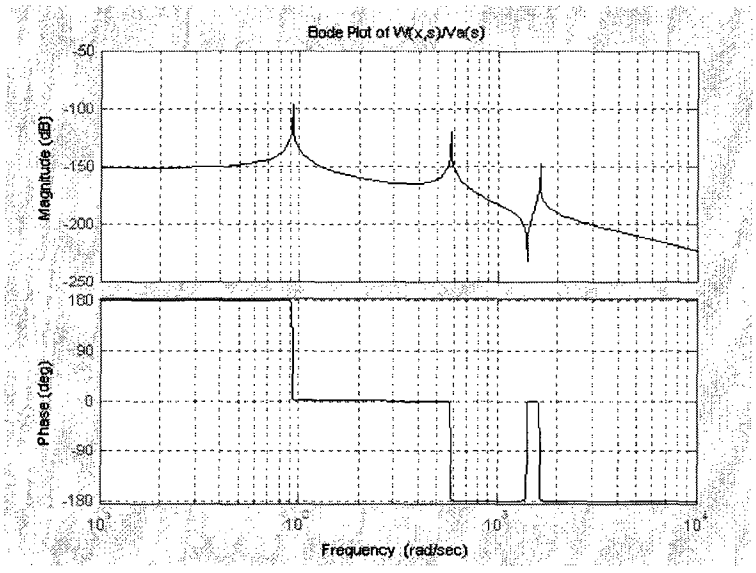

Figure 8. Bode Plot of the Transfer Function of Equation (20).

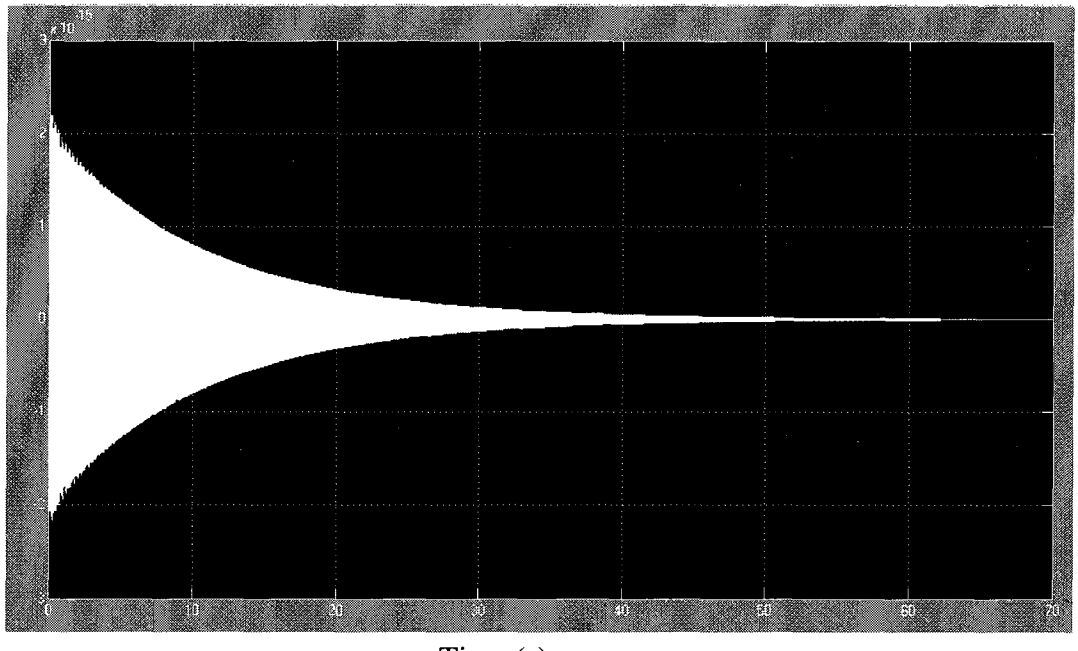

Figure 9. The Impulse Response of the Voltage Sense by the Piezoceramic Material.

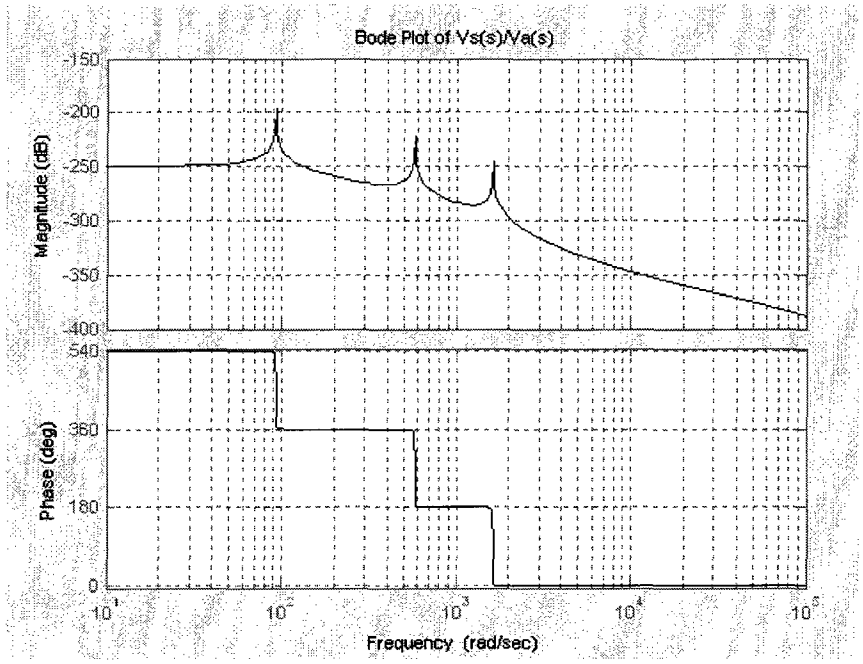

Figure 10. Bode Plot of the Transfer Function Equation (27).

2.8 Parameters of the Piezoceramic Laminate Beam

Table 3 shows the parameters of the aluminum cantilever beam. The properties and locations of the PZT actuators and sensor are shown in Table 4.

Table 3. Parameters of Aluminum 6064 Beam.

Properties	Units	Beam
E (Young Modulus)	lb/in^2	1.09E+07
ρ (density	lb/in^3	0.0975
w (width)	in	0.6
t (thickness)	in	0.065
l (Length)	in	11.8

Table 4. Parameters of PZT PSI-4A4E.

Properties	Units	Sensor	Actuator
d31 (Charge constant)	m/V	-1.90E-10	-1.90E-10
g31 (Voltage constant	Vm/N	-1.16E-02	-1.16E-02
k31 (coupling coef.)	----------	0.35	0.35
ba (width)	in	0.4	0.4
t (thickness)	in	0.0105	0.0105
L (Length)	in	0.5	1
x1(location on Beam)	in	1.5	0
x2(location on Beam)	in	2	1

3. Experimental Setup

The first beam station is constructed based on Griffin's station from *Make* [6]. Griffin's beam station suppressed the vibration of the beam without a microcontroller. A LM324 quad amplifier chip is used for signal processing, derivative control, and as a bridge amplifier. Figure 11 shows a detail circuit schematic of Griffin's beam station.

First the charge signal from the piezoceramic sensor is passed through a charge amplifier in the first operational amplifier circuit. The second operational amplifier in the LM324 serves as a low-pass filter that boosts the input voltage of the first vibration mode. The potentiometer resistance, R2 in Figure 11, is adjusted to match the resonance frequency of the beam. The last two sets of operational amplifiers power the two actuators in tandem. The two bridge amplifiers are then connected to a double pole double throw (DPDT) phase switch. The phase switch can be switched to the up position to suppress the beam vibration or to the down position to excite the beam resonant

vibration. The principle of the up position of the phase switch is to have the actuator function in a 180 degree phase shift to counteract the vibration of the beam [6].

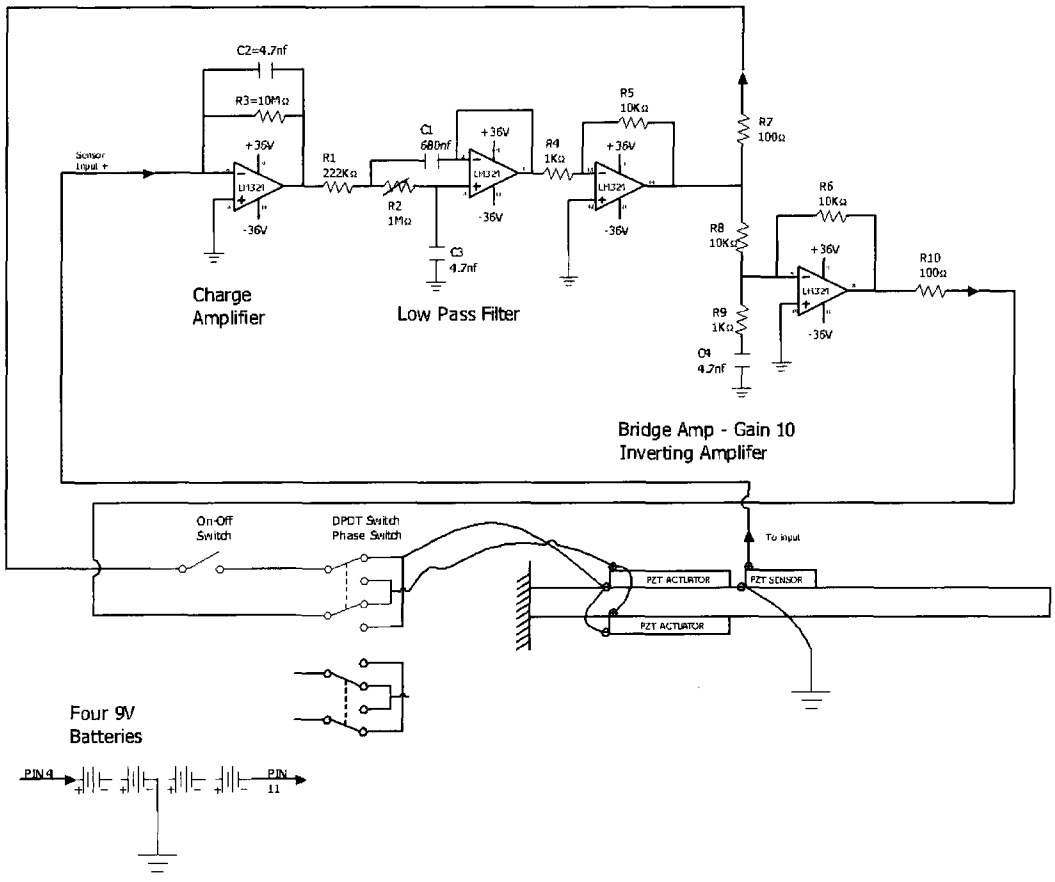

Figure 11. Beam Circuit Detail of LM324 Operational Amplifier.

3.1 Real-Time Experimental Setup with Simulink and Quanser

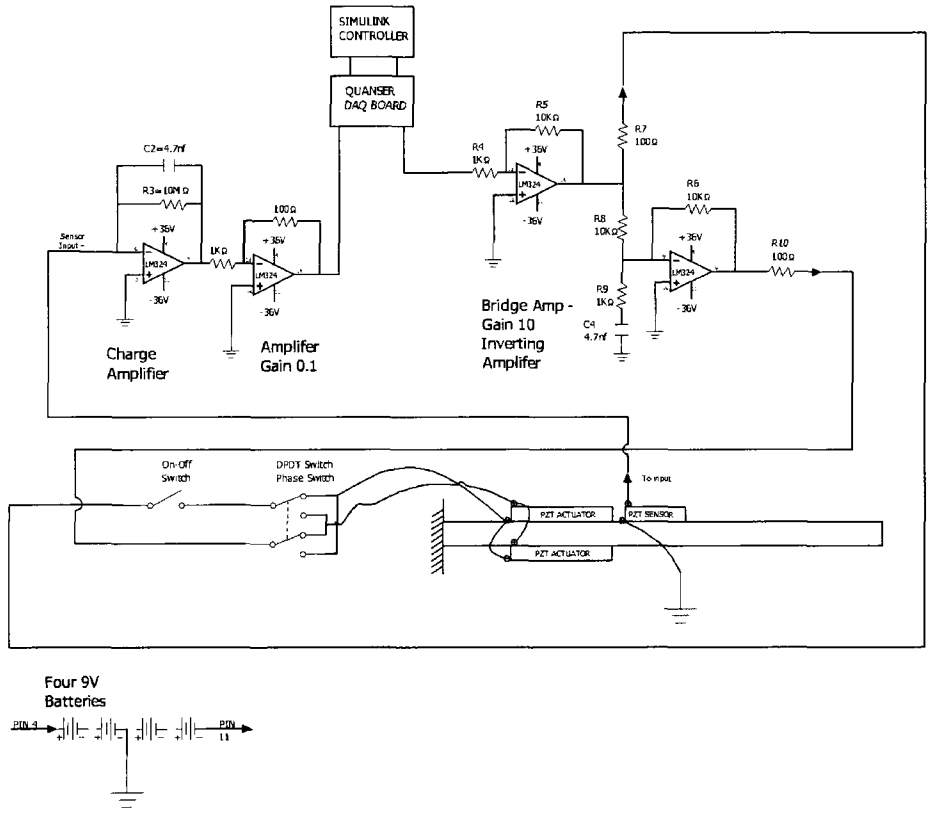

Figure 12. Beam Circuit Interfacing to Quanser between Griffin's Analog Circuit with the Maltab-Quanser System.

Figure 12 shows the connection between Griffin's beam station and real-time with the Matlab-Quanser system. Figure 12 shows the second amplifier with a gain of 0.1 which replaces the low pass filter, as shown in Figure 11. The 0.1 gain amplifier attenuates the input voltage and its output voltage is sent to Simulink-Quanser data acquisition board. The output signal from the Simulink control block unit is multiplied by a gain of 10 from the amplifier.

3.1.1 Real-Time Hardware Setup

The real-time experimental setup of the beam station is shown in Figure 13. Figure 14-16 show a close-up view of the cantilevered beam along with actual PZT actuators and sensor. Figure 17 shows the analog input and output signal connection to the Quanser DAQ board.

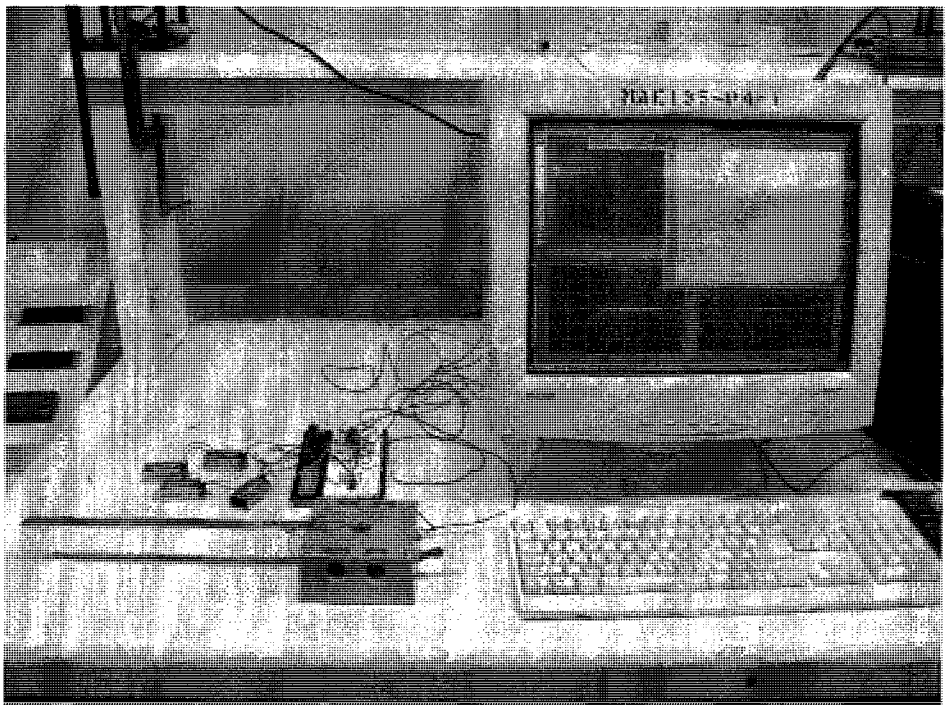

Figure 13. Experimental Beam Station Connected to Simulink-Quanser.

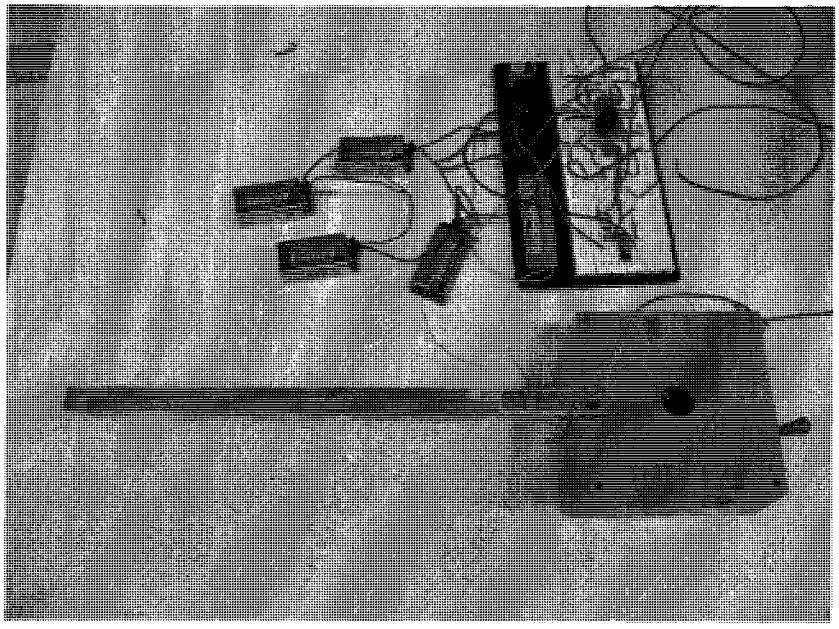

Figure 14. View of Beam Station and Circuit.

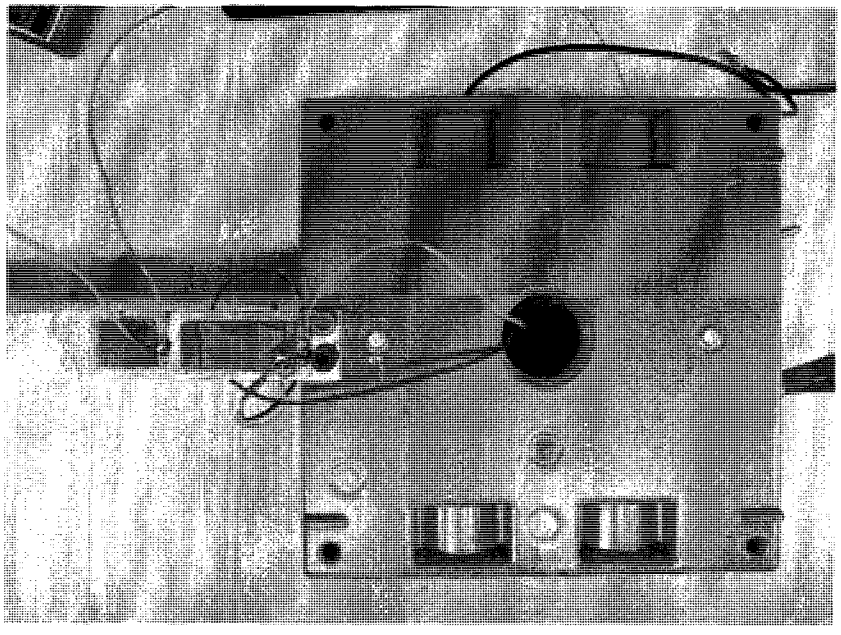

Figure 15. Close Up Top View of Beam Station Showing Piezoceramic Actuator and Sensor.

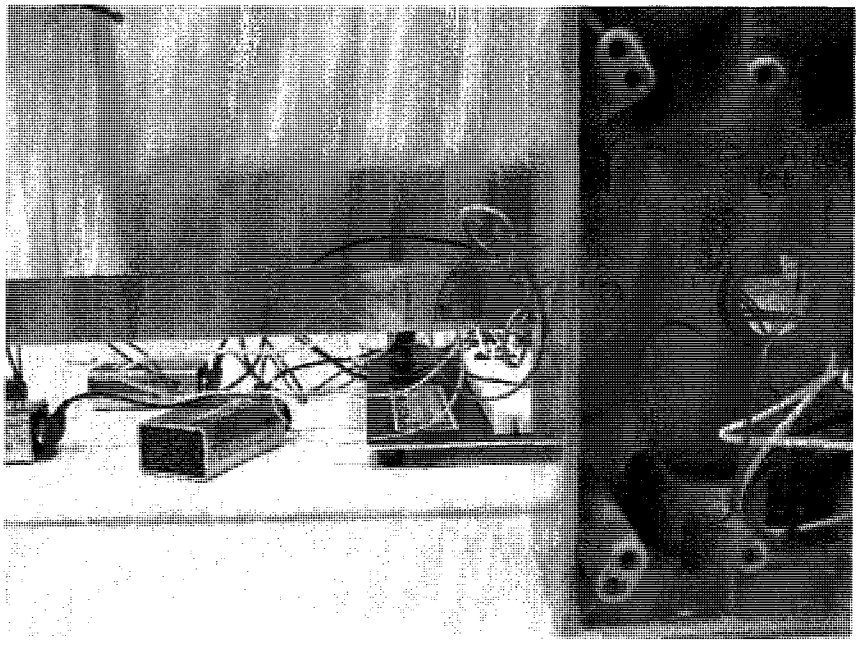

Figure 16. Close Up Bottom View of Beam Station Showing Piezoceramic Actuator .

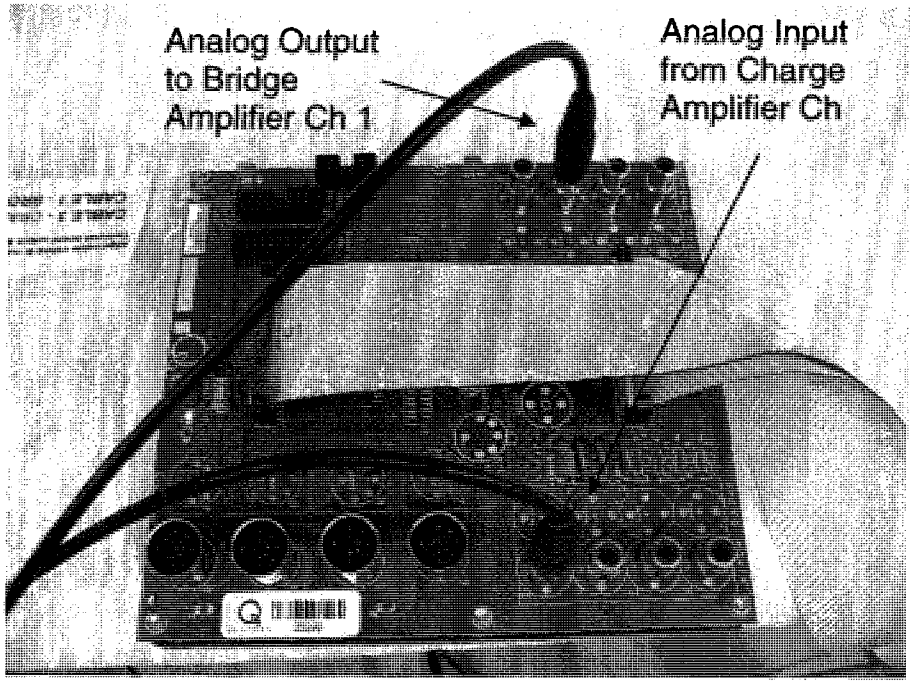

Figure 17. Quanser DAQ Board with Analog.

3.2 Experimental Identification

The first experimental study was to examine the open loop beam vibrations. The experimental setup is shown in Figure 12. The beam was manually deflected by the operator at the free end of the beam with a tip deflection of approximately 1 inch. With the PZT sensor and the charge amplifier connected to the Quanser DAQ board, the open loop response of the beam was examined. The damping parameter was identified to be $\zeta_1 = 0.005$ in Equation (27). The damping parameters for $\zeta_{2,3}$ was approximated to be 0.001 in this study.

It takes approximately 40s for the beam to settle without the lamination of sensor and actuators on the beam. The lamination of the PZTs significantly decreases the settling time of the beam to approximately 7.7s as shown in Figure 20. Due to the inconsistency of tip deflection of the beam from using a finger, the vibration response peak voltage is not the same in each measurement in real-time control implementation. Therefore, a method is imposed to measure the settling time of each vibration response case without bias. The settling time in this study is defined as

$$T_{settling} = T_{V=0.1} - T_{V=10} \tag{27a}$$

where $T_{V=0.1}$ is the time where the vibration level will be less than 0.1V for $t > T_{V=0.1}$. Figure 20 shows a visual detail for $T_{settling}$.

The natural frequency of the first mode matched well with the experimental and analytical results. The sampling time of the Quanser DAQ board is limited to 100 Hz. Therefore only the first two modes of the beam vibration could be evaluated for system

identification and vibration control. An experimental method to verify the first two modal frequencies of the beam is to excite the structure and examine its resonance response, as seen in Figure 19. For the first mode, the resonant frequency was observed to be at 97.5 rad/s. Similarly, the second mode was observed to be 589.7 rad/s.

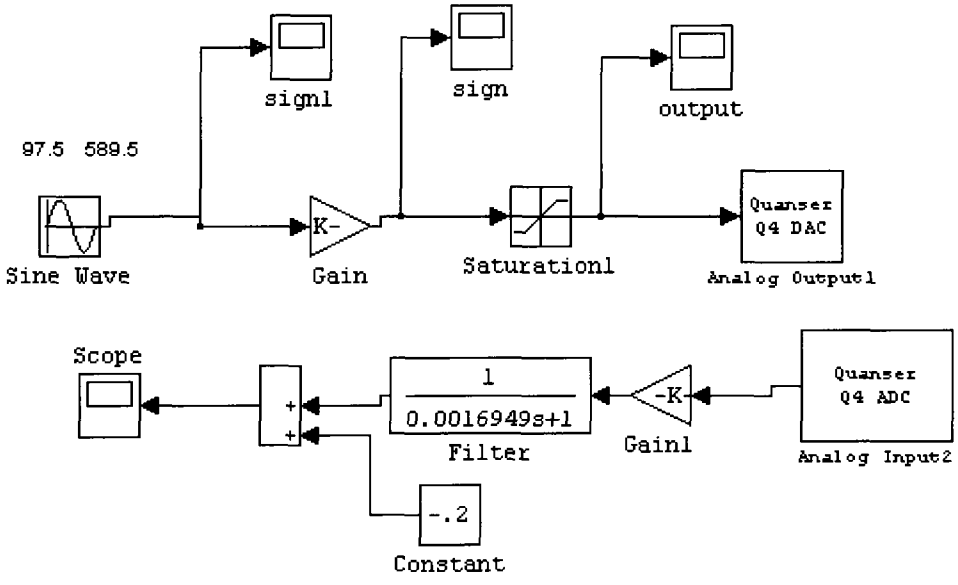

Figure 18. Real-Time Implementation of Open Loop Actuation at the Beam Natural Frequency.

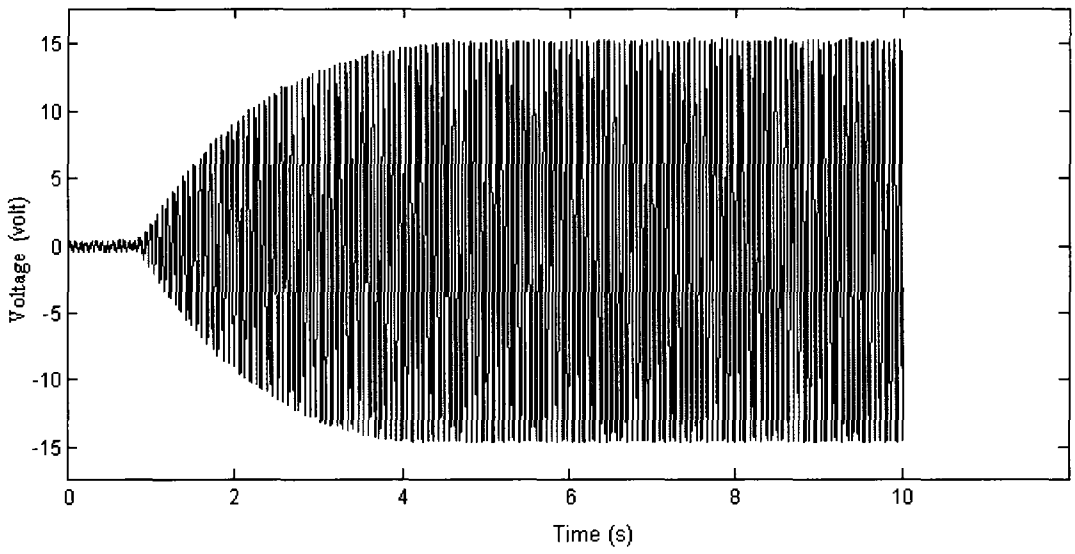

Figure 19. Plot of Open Loop Actuation at Resonant Frequency of 97.5 rad/s.

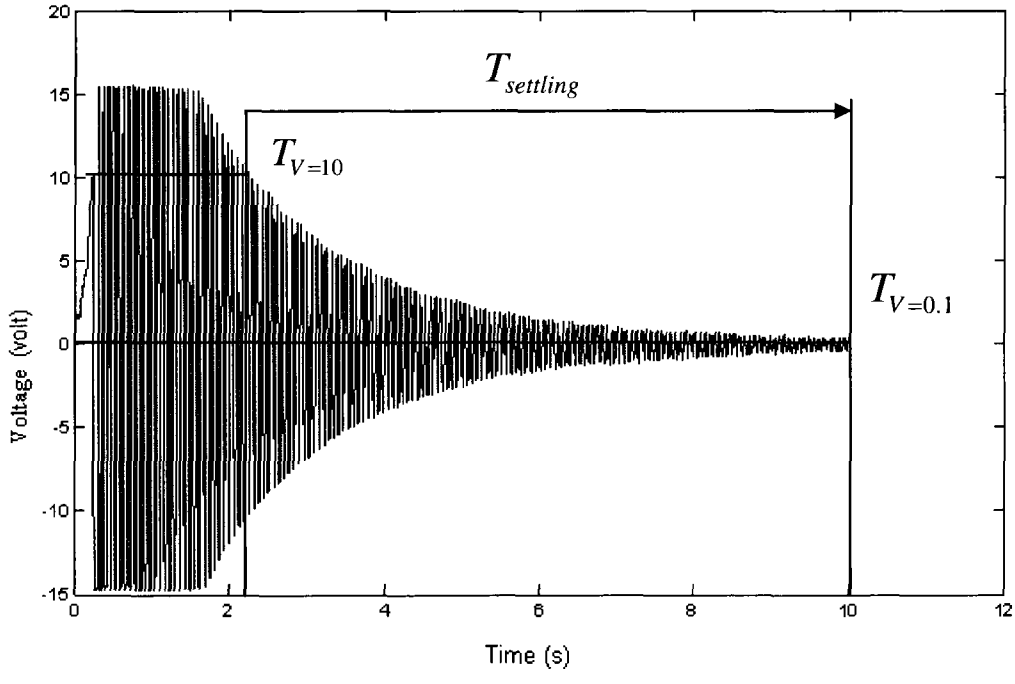

Figure 20. Open Loop Reponse of Beam Deflected at Approximately 1 inch.

The damping parameter for the first mode is calculated in Equation (27.2) from [5]. Figure 21 is a close up view of Figure 20 and it provides the data points to calculate the damping parameter in Equation (27.2).

$$\zeta_1 = \frac{1}{2\pi 10}\ln\left(\frac{A_1}{A_0}\right) = \frac{1}{2\pi 10}\ln\left(\frac{3.946}{2.848}\right) = 0.0052 \tag{27.2}$$

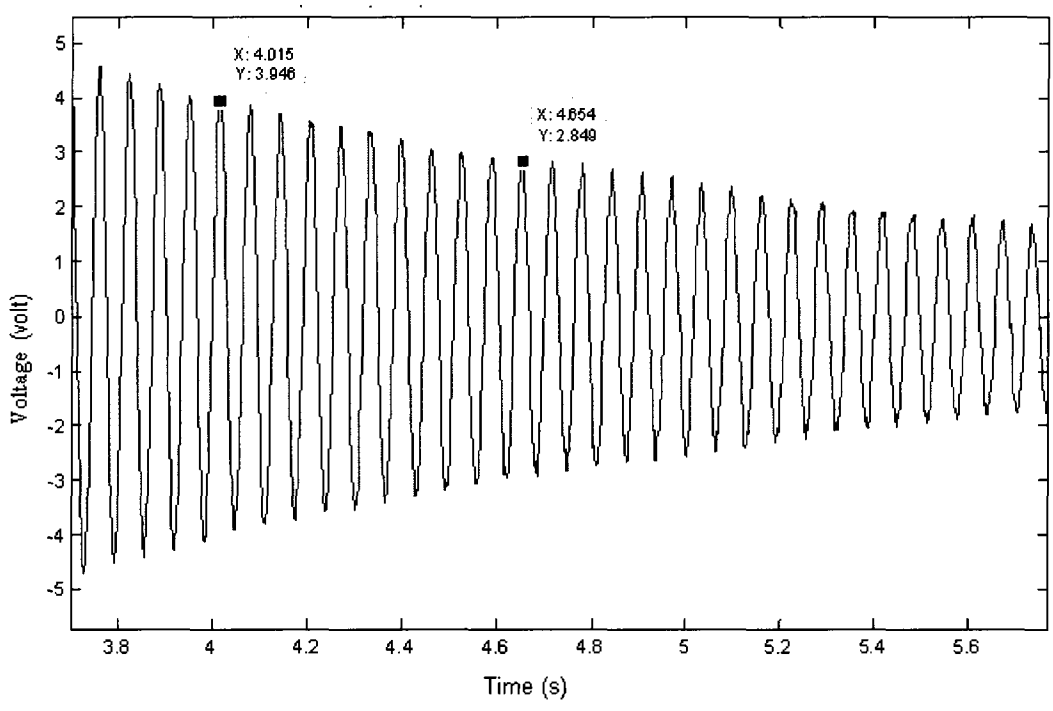

Figure 21. Plot to Calculate Damping Coefficient of First Mode Open Loop Response.

4. Vibration Control Method

Three control methods that have been successfully implemented to suppress the vibration of the beam in this study. The first method of active control comes from

Griffin's analog circuit. The second method of active control is the Proportional and Derivative (PD) control with the modified Griffin's circuit. Simulink in PD simulation and real-time control was implemented. The third method of active control is the state feedback with a full state observer. A linear quadratic regulator (LQR) optimal control method was implemented for vibration suppression in simulation study and real-time control.

4.1 Method 1: Derivative Control

The derivative control method uses the low pass filter as shown in Figure 11 to filter the high frequency vibration of the beam, allowing only the first modal vibration of 15.5 Hz to pass through. In addition to low pass filtering, this filter also provides the derivative of the input signal for derivative control action. This control method is in the form of

$$V_a = -K\frac{dV_s}{dt} \tag{27.3}$$

where K is the control gain, and $\frac{dV_s}{dt}$ is the derivative of the voltage signal from the sensor.

Figure 22 shows the result of the active derivative control of the beam. From Figure 22, the vibration observed ($V_s(t)$) is considerably reduced within the first 1.5s. After 1.5s, there is still some minimal vibration that lasts for another 2s until the beam completely settles to 0V.

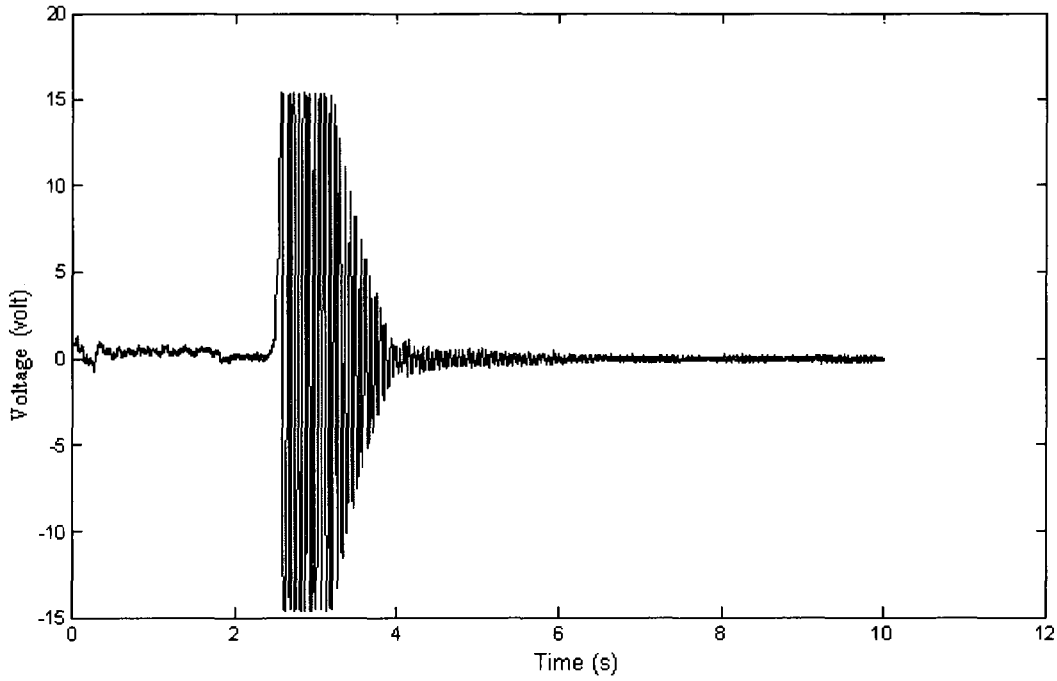

Figure 22. Derivative Controller of *Make* Analog Circuit.

4.2 Method 2: Proportional and Derivative Control, PD Controller

An impulse open loop response is simulated as seen in Figure 23 and plotted in Figure 24. Then the PD beam vibration control system is investigated. The PD controller provides good damping in the beam vibration, resulting in 1s settling time in the simulation study with P=40 and D=1.5, and 2.25s settling time for real-time control with P=17 and D=0.01.

4.2.1 PD Controller Simulation

Figure 23 shows the Simulink diagram for the open loop response. Figure 24 shows the simulated open loop response.

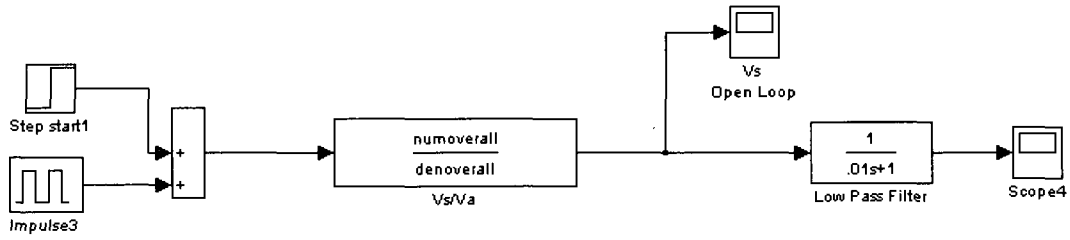

Figure 23. Simulink Open Loop Response Simulation of Transfer Function for First Three Modes.

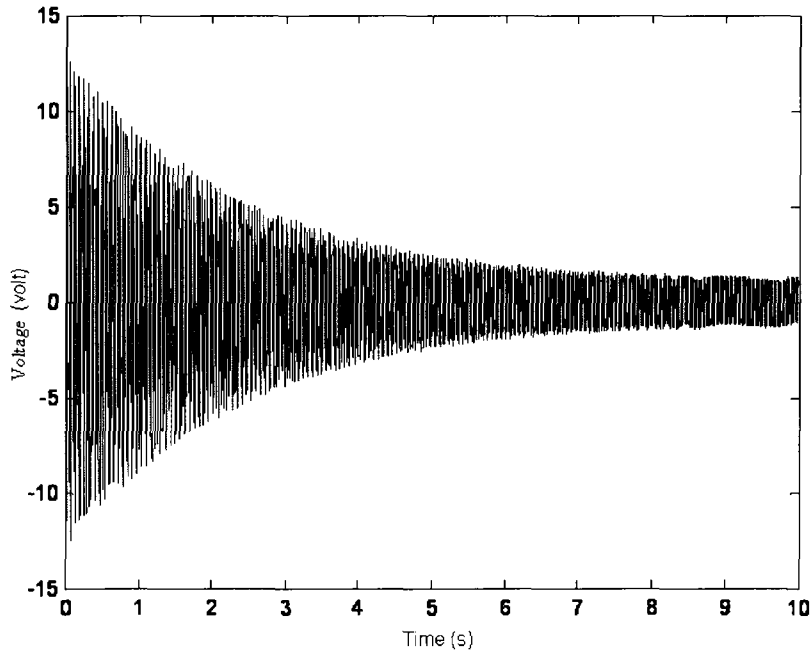

Figure 24. Plot of Simulink Open Loop Response Simulation.

The PD control Simulink simulation is shown in Figure 25. The low pass filter with bandwidth of 100 rad/s passes only the first mode of beam vibration to the feedback loop. Essentially, the PD controller is only damping the first mode of vibration. If there is no low pass filter, the noise and the higher frequency modal vibration are amplified with the derivative action, causing instability in the beam vibration. The best PD controller gains were found to be at P=40, and D=1.5, as shown in Figure 26. Figure 27 shows the simulation case with P=17 and D=0.01. The best settling time for PD control simulation is 1s.

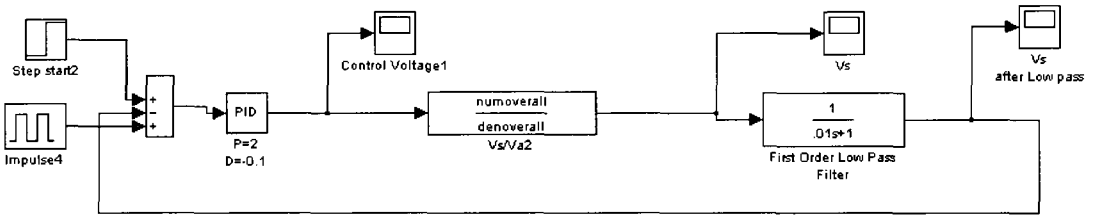

Figure 25. PD Controller Simulation of Beam Vibration Suppression.

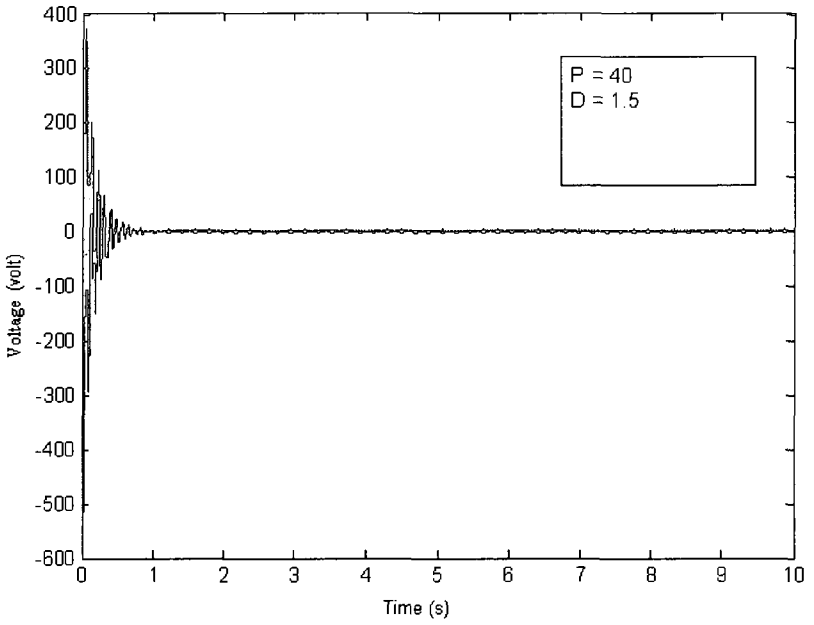

Figure 26. PD Vibration Suppression Simulation, P=40, D=1.5.

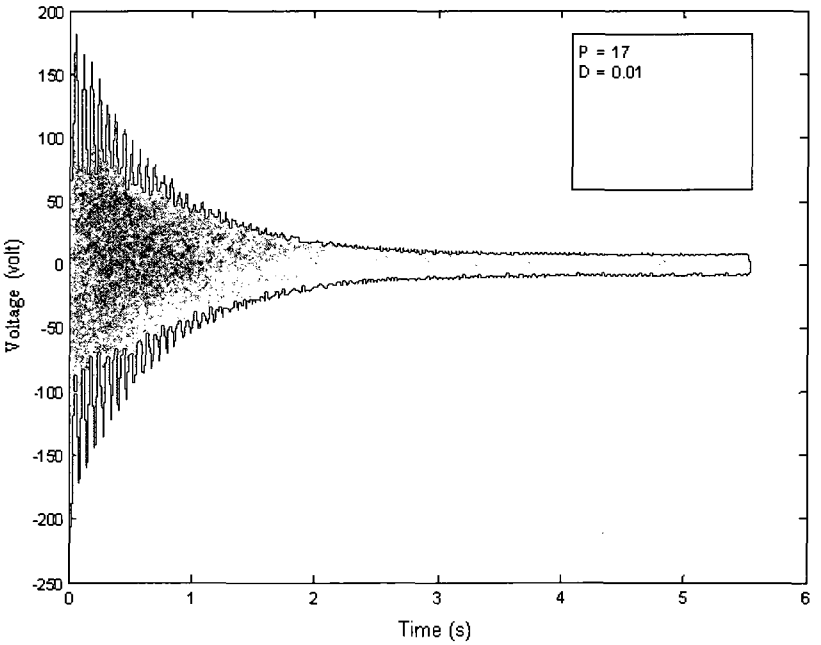

Figure 27. PD Vibration Suppression Simulation, P=17, D=0.01.

4.2.2 PD Real-Time Control

A simulation implementation of the real-time digital PD control in Simulink is shown in Figure 28. The sensor voltage is connected to the Quanser analog input box. The signal goes through a series of signal conditioning units: first a low pass filter, an offset constant unit and then an amplifier with the gain of 10. Then the signal is fed back for PD control. Figure 29 and Figure 30 show the real-time PD control beam vibration and the control voltage with P=17 and D=0.01 with a settling time of 2.25s. The maximum sensor voltage in Figure 29 is much less than that of the PD simulation in Figure 26 due to real-time hardware limitation.

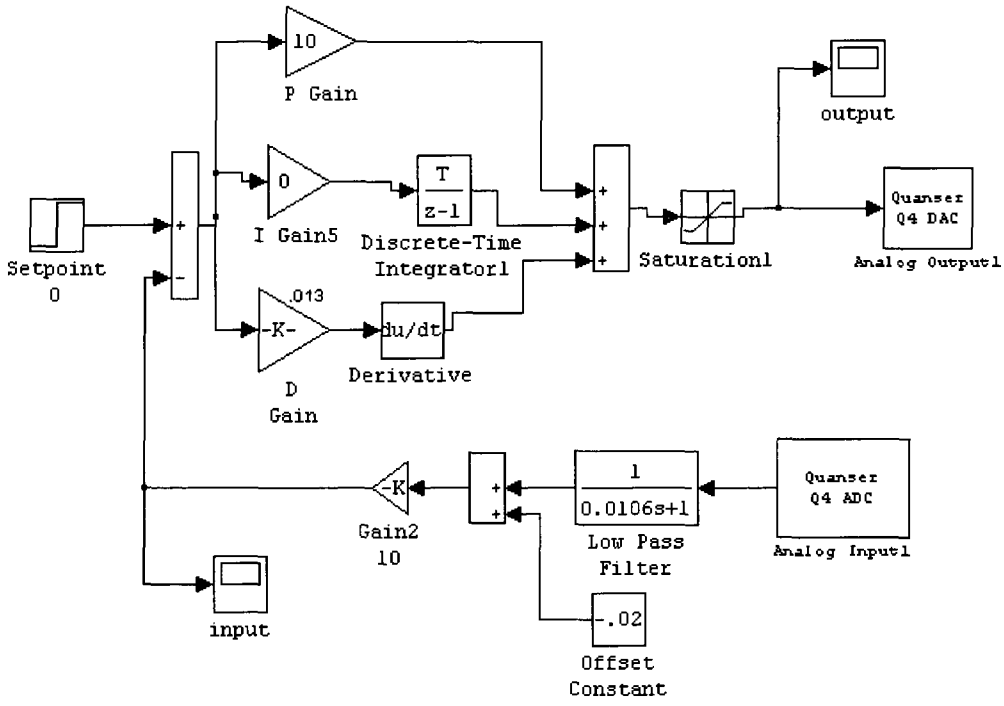

Figure 28. Real-Time PD Controller Implementation Block Diagram Simulink.

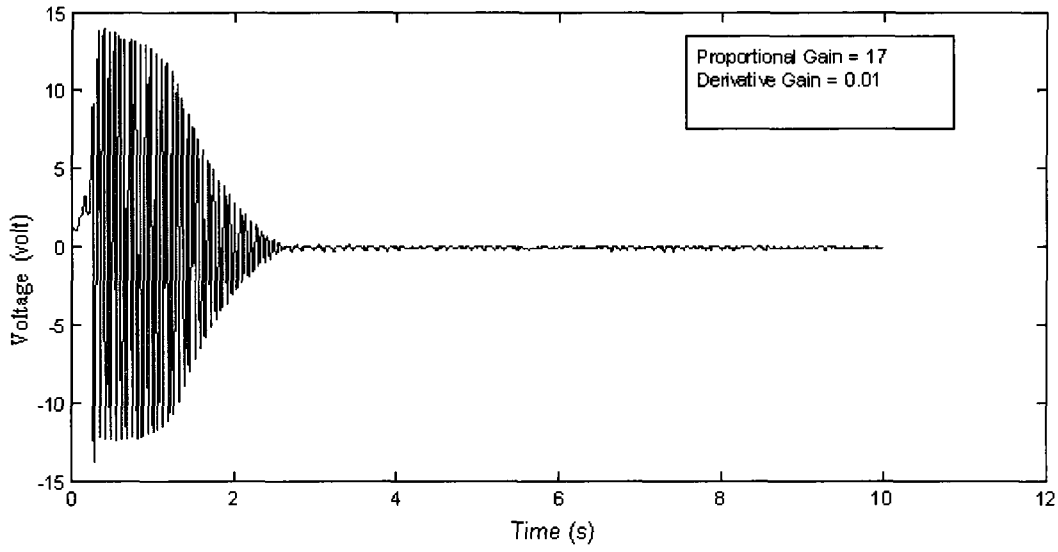

Figure 29. Real-Time Plot of PD Vibration Suppression, P=17, D=0.01.

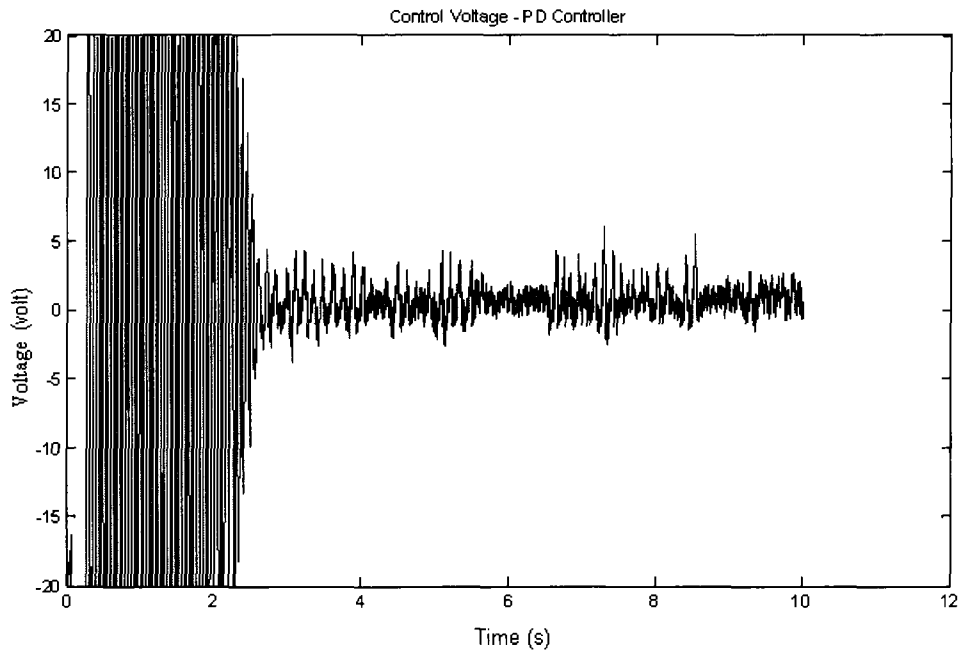

Figure 30. Real-Time Plot of Control Voltage.

4.3 Method 3: LQR State Feedback with Observer Design- LQR Controller

4.3.1 State Space Dynamic Model Derivation

From Equation (27), the transfer function is transformed to a state space vector dynamic equation for state feedback control system design. Since the first two modes are dominant, and due to the limitation of sampling rate of the Quanser DAQ board of 100 Hz, only the first two modes of the transfer function in Equation (27) will be considered for state space base optimal control. A second order transfer function for each mode requires two state variables. There are two modes and one input, so a 4 by 4 system A matrix and a 4 by 1 system input matrix is needed. The output y matrix is the sensor voltage, and is a combination of the state from the first mode and second mode of the beam bending vibration. The state variables are in the form

$$\begin{aligned} x_1 &= \eta_1(t) \\ x_2 &= \dot{\eta}_1(t) = \dot{x}_1 \\ x_3 &= \eta_2(t) \\ x_4 &= \dot{\eta}_2(t) = \dot{x}_3 \end{aligned} \tag{28}$$

where the state space matrix dynamic model is in the form

$$\begin{aligned} \dot{x} &= Ax + BV_a \\ y &= Cx \end{aligned} \tag{28a}$$

The details of the A, B, and C matrices are in Equation (28a) and shown as

$$\begin{bmatrix} \dot{x}_1 \\ \dot{x}_2 \\ \dot{x}_3 \\ \dot{x}_4 \end{bmatrix} = \begin{bmatrix} 0 & 1 & 0 & 0 \\ -\omega_{n1}{}^2 & -2\zeta_1\omega_{n1} & 0 & 0 \\ 0 & 0 & 0 & 1 \\ 0 & 0 & -\omega_{n2}{}^2 & -2\zeta_2\omega_{n2} \end{bmatrix} \begin{bmatrix} x_1 \\ x_2 \\ x_3 \\ x_4 \end{bmatrix} + k_a \begin{bmatrix} \phi_1'(x_{a2}) - \phi_1'(x_{a1}) \\ 0 \\ \phi_2'(x_{a2}) - \phi_2'(x_{a1}) \\ 0 \end{bmatrix} V_a(t) \tag{28b}$$

$$y = \frac{k_s}{C_s b_s (x_{s2} - x_{s1})} \begin{bmatrix} \phi_1'(x_{s2}) - \phi_1'(x_{s1}) & 0 & \phi_2'(x_{s2}) - \phi_2'(x_{s1}) & 0 \end{bmatrix} \begin{bmatrix} x_1 \\ x_2 \\ x_3 \\ x_4 \end{bmatrix}$$

4.3.2 Observability and Controllabilty

Observability and controllability of the state space dynamic model are examined to prove whether the system is state controllable and state observable. The following relationships give the controllability matrix Co

$$Co = (B, AB, A^2B, ..., A^{n-1}B) \tag{29}$$

where A and B are the state space matrices of the system. The matrix Co must be full rank to be state controllable. Controllability is calculated in Matlab with the obsv and rank command.

$$\begin{aligned} Co &= obsv(A, B) \\ Controllability &= rank(Co) \end{aligned} \tag{30}$$

The observability matrix is given by

$$O = (C^T, A^T C^T, ..., (A^T)^{n-1} C^T) \tag{31}$$

where C is the output state space matrix of the system. Observability is calculated in Matlab with the following command

$$ob = obsv(A, C)$$
$$observability = rank(ob) \tag{31a}$$

The duality between the observer design and the state feedback regulator design allows for an observer design with the transpose of the A and the C matrix. In this study, the observability and controllability matrix are full rank. Full rank is the maximum number of linearly independent columns of the matrix A. The observer design was based on the pole placement method. The observer gain is calculated with the Matlab command in Equation (32) and Equation (32a).

$$K_e = place(A', C', po) \tag{32}$$

where,

$$po = \text{the desired poles location} \tag{32a}$$

4.3.3 Observer Design

An observer design is required since all 4 states cannot be individually measured. The separation principle allows the design of the observer to be independent from the design of the state feedback regulator. The full state observer is in the form of Equation (33)

$$\dot{\hat{x}} = A\hat{x} + Bu + K_e\left(y - \hat{y}\right) \tag{33}$$

where

$$\begin{aligned} y &= Cx \\ \hat{y} &= C\hat{x} \\ u &= V_a \end{aligned} \tag{34}$$

$$\begin{aligned} \dot{\hat{x}} &= \left(A - K_e c\right)\hat{x} + Bu + K_e y \\ \dot{\hat{x}} &= A_{ob}\hat{x} + \begin{bmatrix} B & K_e \end{bmatrix}\begin{bmatrix} u \\ y \end{bmatrix} \\ \dot{\hat{x}} &= A_{ob}\hat{x} + B_{ob}\begin{bmatrix} u \\ y \end{bmatrix} \end{aligned} \tag{35}$$

where $\hat{x}$ is the estimated state, and $\hat{y}$ is the estimated output. For this flexible beam system, the eigenvalues of the observer matrix are assigned as

-5.0000 + 2.0000i, -5.0000 - 2.0000i, -1.0000 + 1.0000i, -1.0000 - 1.0000i

with observer gain (K_e) of

$$\left[0.0007, -0.6349, -0.0120, 405.7231\right]^T$$

4.3.4 LQR State Feedback Gain

Similar to the observer design, the separation and the duality principle applies to the LQR design. The state space system in Equation (28a) is controllable. Therefore, there is a linear state feedback gain (k) that can be found such that the quadratic cost function (J) is minimized.

$$J = \int_0^\infty \left(x^T Q x + v' R V_a \right) dt \tag{36}$$

where

$$Q = \alpha \begin{pmatrix} 1 & 0 & 0 & 0 \\ 0 & 1 & 0 & 0 \\ 0 & 0 & 1 & 0 \\ 0 & 0 & 0 & 1 \end{pmatrix} \tag{37}$$

$$R = \beta \tag{38}$$

where α and β are scalar value.

The Matlab command in Equation (39) is used to compute the LQR gain matrix.

$$[k, S, E] = lqr(A, B, Q, R) \tag{39}$$

The control voltage (V_a) is generated in the form of

$$V_a = -kx$$

4.3.5 LQR State Feedback Controller Simulation

The open loop response (Figure 32) is simulated in Simulink (Figure 31) to verify that the model is close to the experimental open loop response. With the observer

designed separately, the LQR feedback controller gain matrix was calculated via Matlab command with Equation (39). Different combinations of α and β in the Q and R weighting matrices were evaluated to find the response with the best settling time. Figure 33 shows the complete LQR base control system in Simulink form.

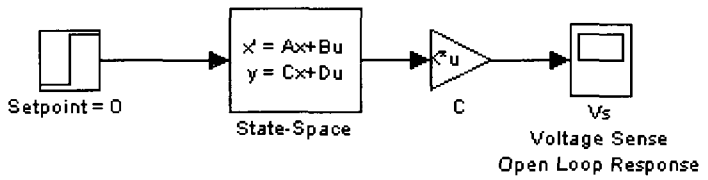

Figure 31. State Space Open Loop Response with Initial Condition.

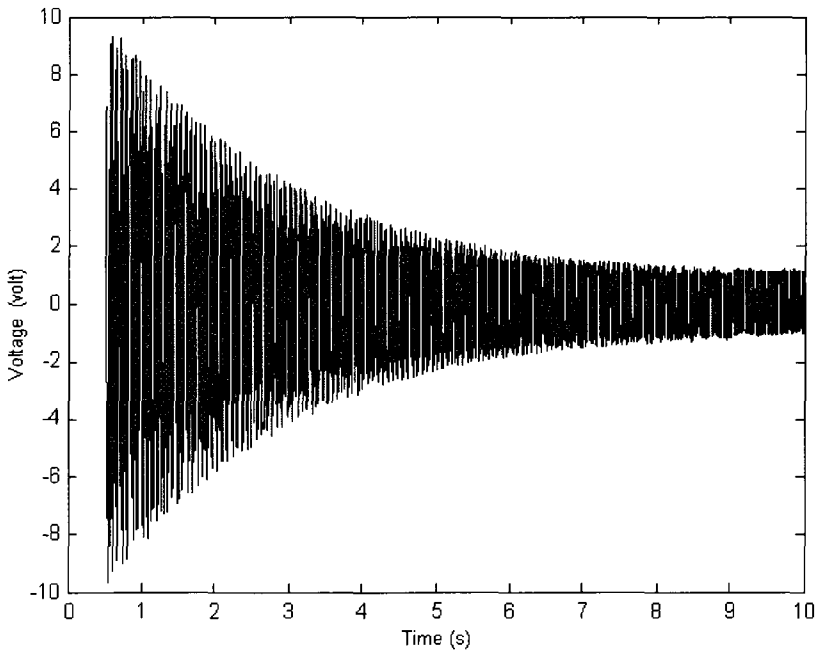

Figure 32. Plot of State Space Open Loop Response with Initial Condition [.01 0 .01 0].

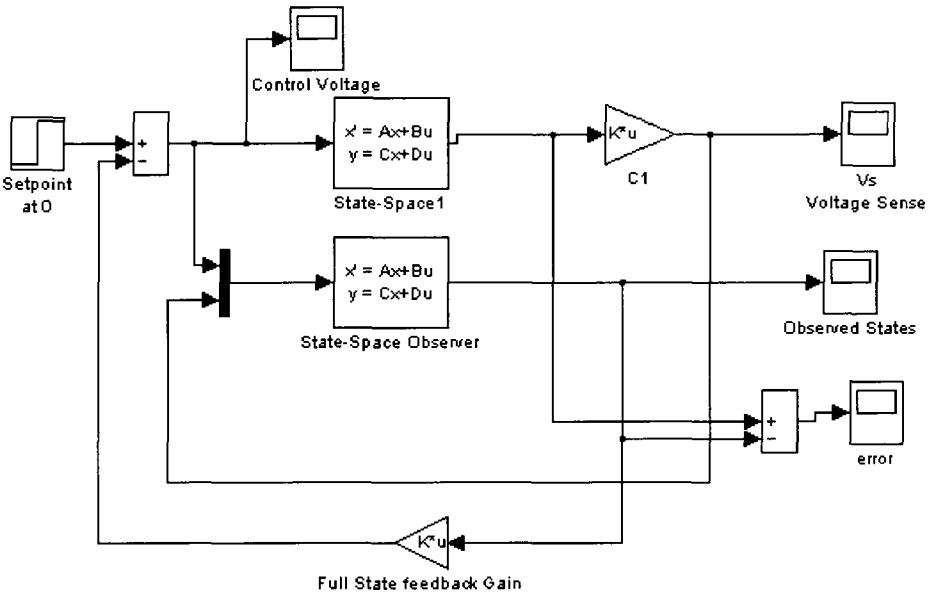

Figure 33. State Space with Observer and LQR State Feedback Simulink Simulation.

Some of the Simulink simulation results of the LQR control system are shown in Figures 34-42.

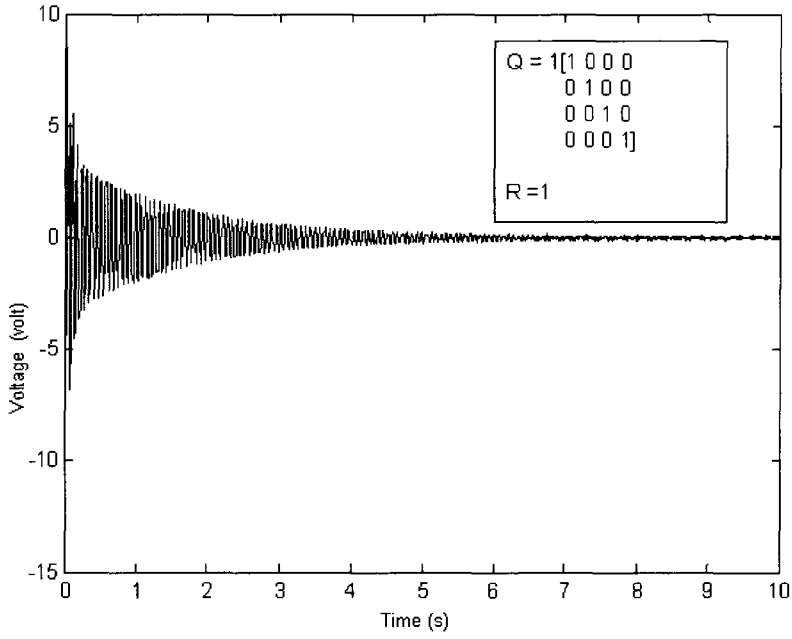

Figure 34. Voltage Sense of LQR Controller at α=1, β=1.

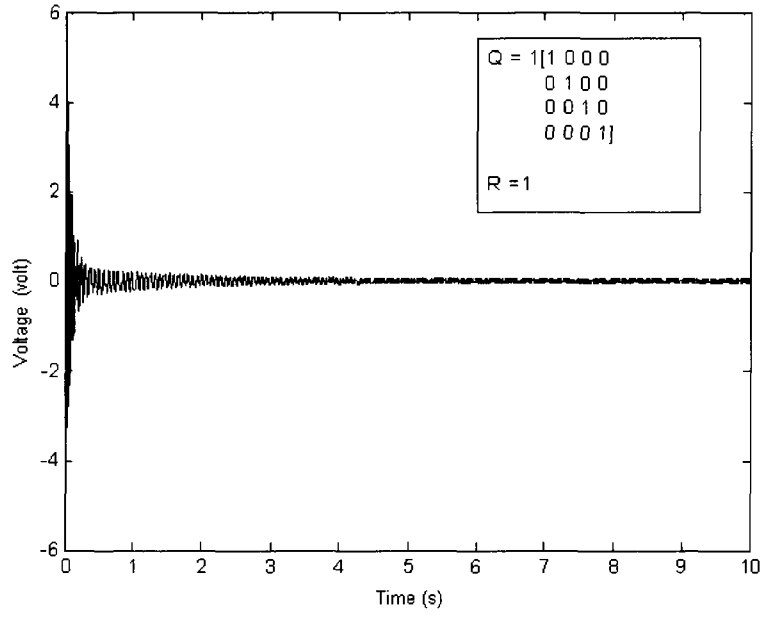

Figure 35. LQR Control Voltage at α=1, β=1.

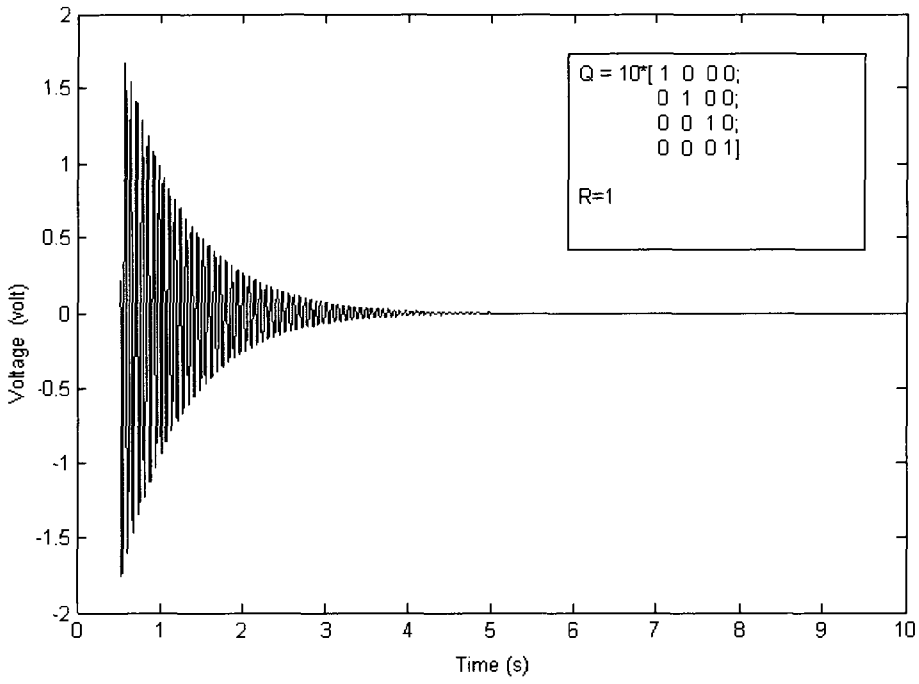

Figure 36. Voltage Sense of LQR Controller at α=10, β=1.

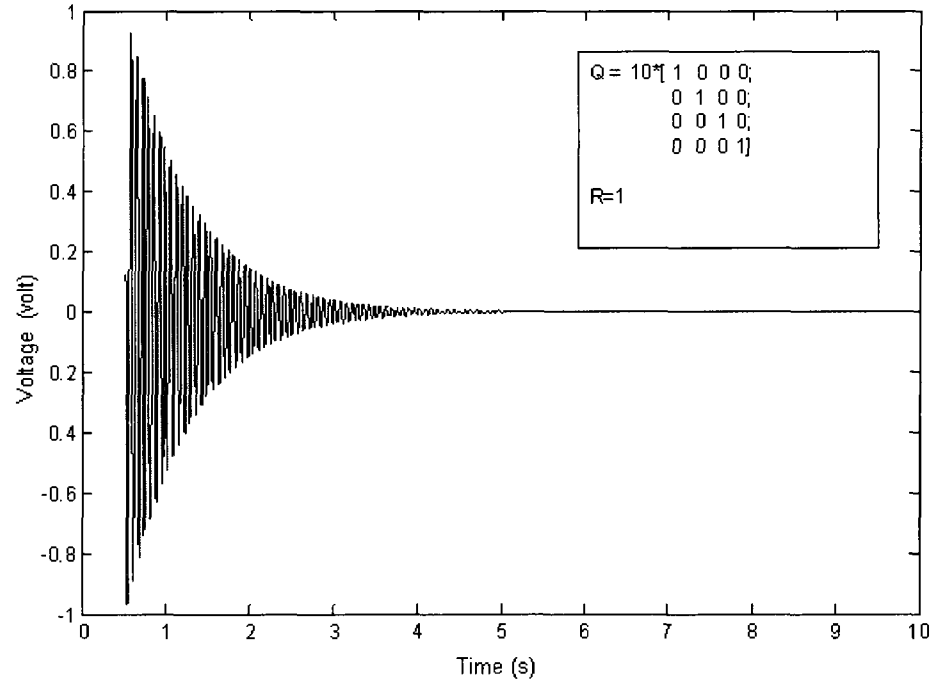

Figure 37. LQR Control Voltage at α=10, β=1.

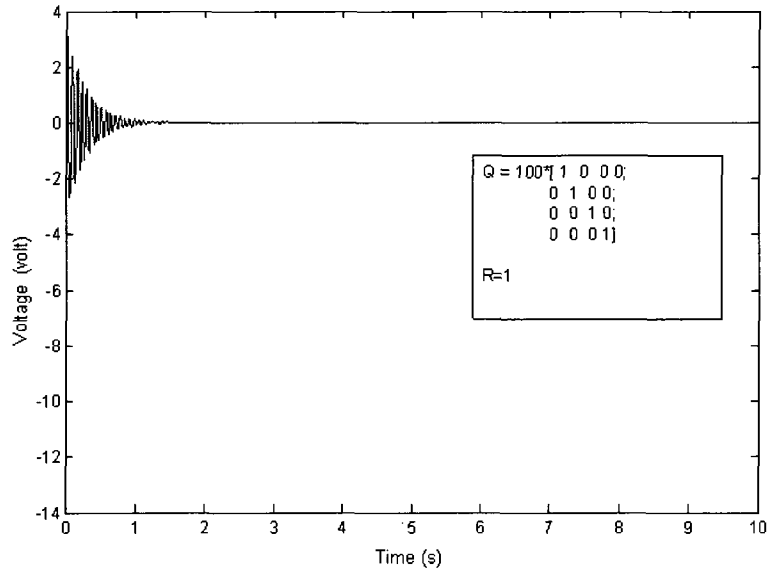

Figure 38. Voltage Sense of LQR Controller at α=100, β=1.

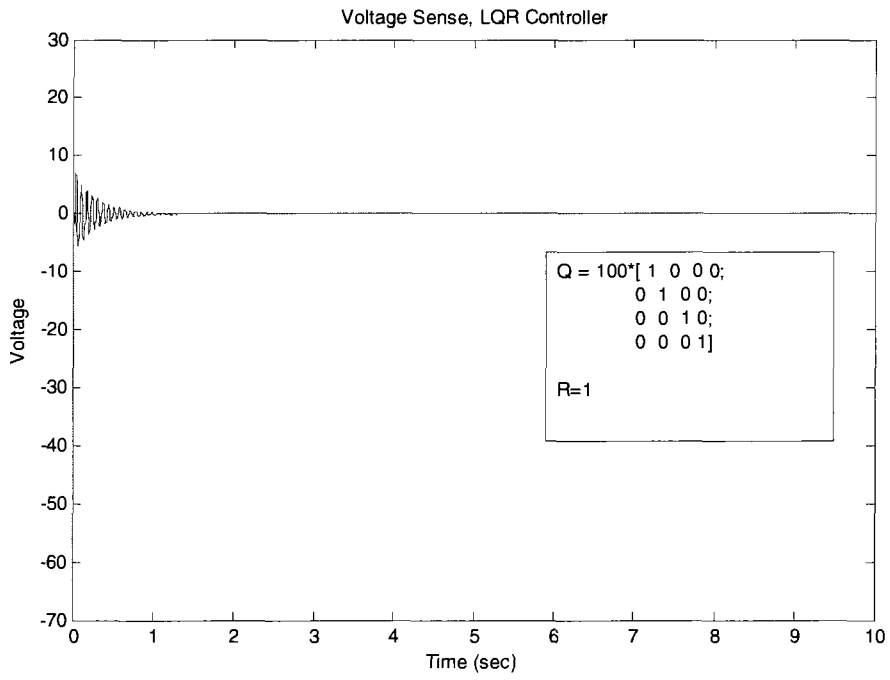

Figure 39. LQR Control Voltage at α=100, β=1.

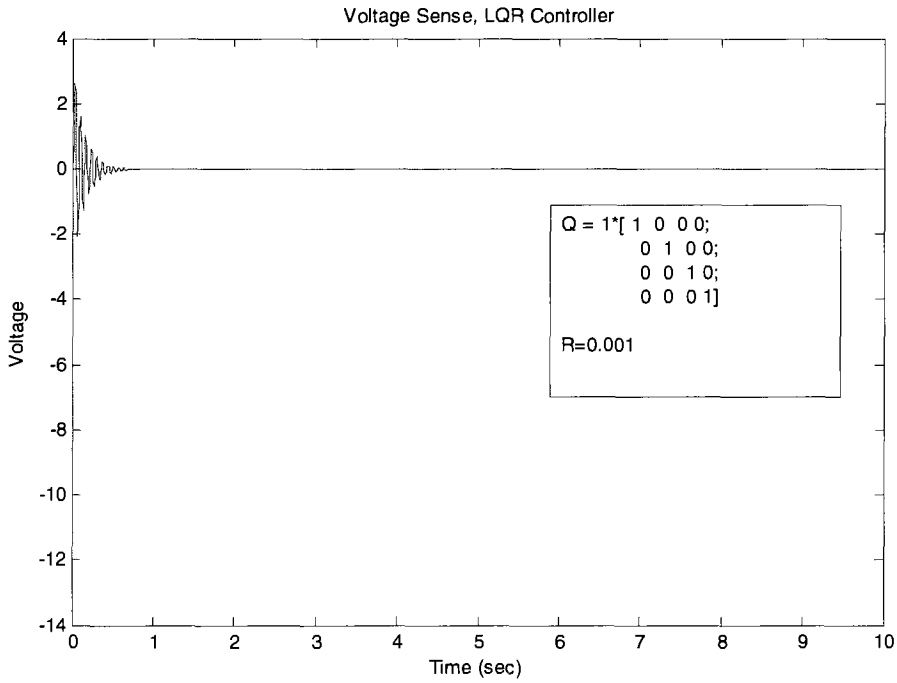

Figure 40. Voltage Sense of LQR Controller at α=1, β=0.001.

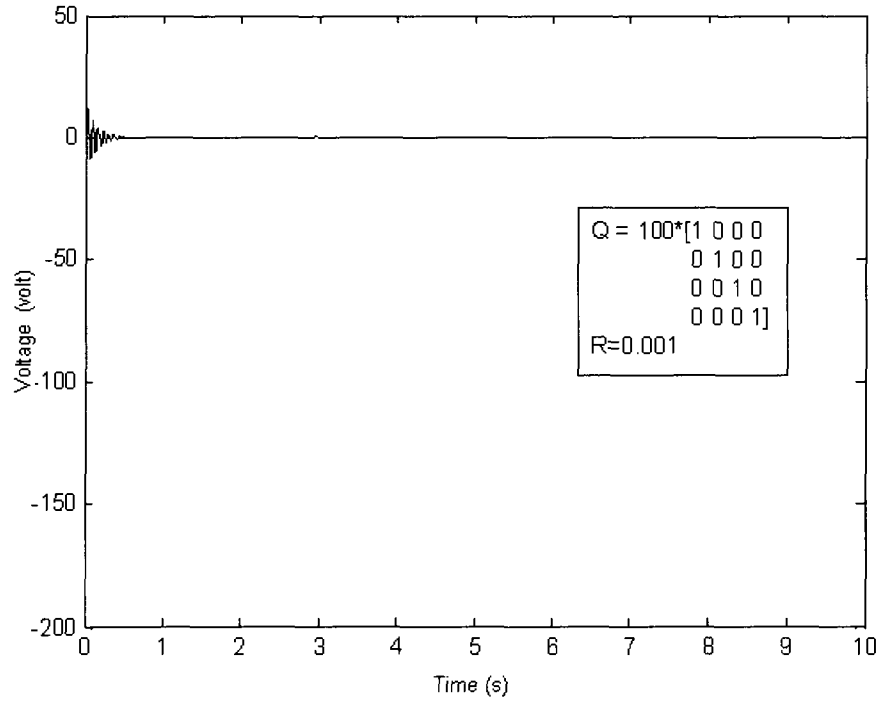

Figure 41. LQR Control Voltage at α=1, β=0.001.

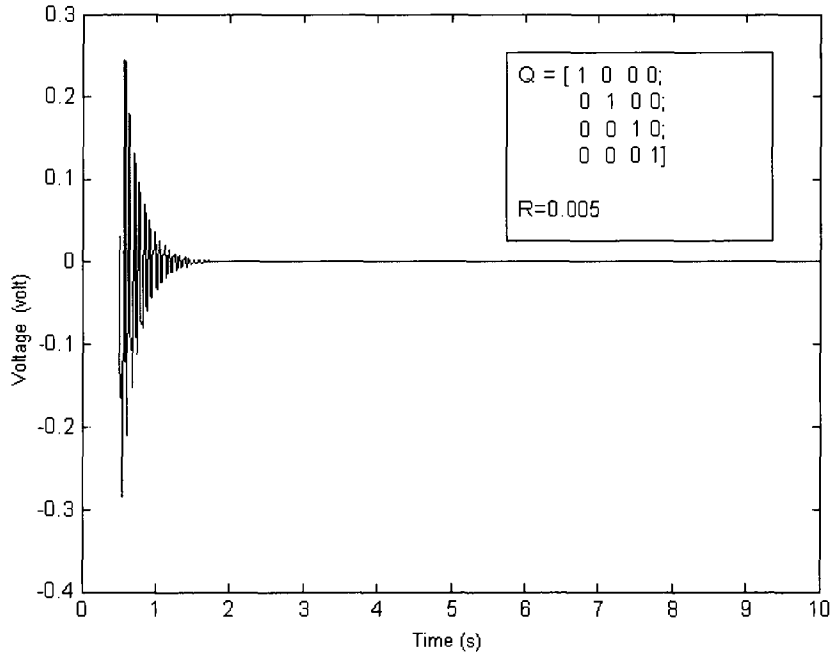

Figure 42. Voltage Sense of LQR Controller at α=1, β=0.005.

The increase of α in the Q matrix from α = 10 in Figure 36 to α = 100 in Figure 38 significantly dampens the beam vibration from 4.5s to 1.5s settling time with low control voltage of 8V. The decrease of β from 1 to 0.001 also significantly dampens the beam vibration from 6s settling time to 0.7s. However, there is an increase in the maximum control voltage from 5V volt to 175V. In real-time implementation 175V is not feasible. The maximum voltage could be applied to the PZT actuator is ±90V. The actual hardware configuration shown in Figure 12 has a limited control output voltage (V_a) of ±36V.

4.3.6 LQR Real-Time Control

The LQR controller implementation setup in real-time is shown in Figure 43. It is important to note that the sensor voltage signal is signal conditioned by a first order low pass filter with the time constant of T = 0.0109s. The voltage signal is offset to 0V and multiplied by a gain of 10 because there is an operational amplified signal with a gain of 0.1 before the signal goes to the DAQ board. Similar to the simulation in Figure 33, the sensor voltage and the actuator control voltage input to the state observer. The observer estimated states vector is multiplied by the computed LQR full state feedback gain (k) for control action.

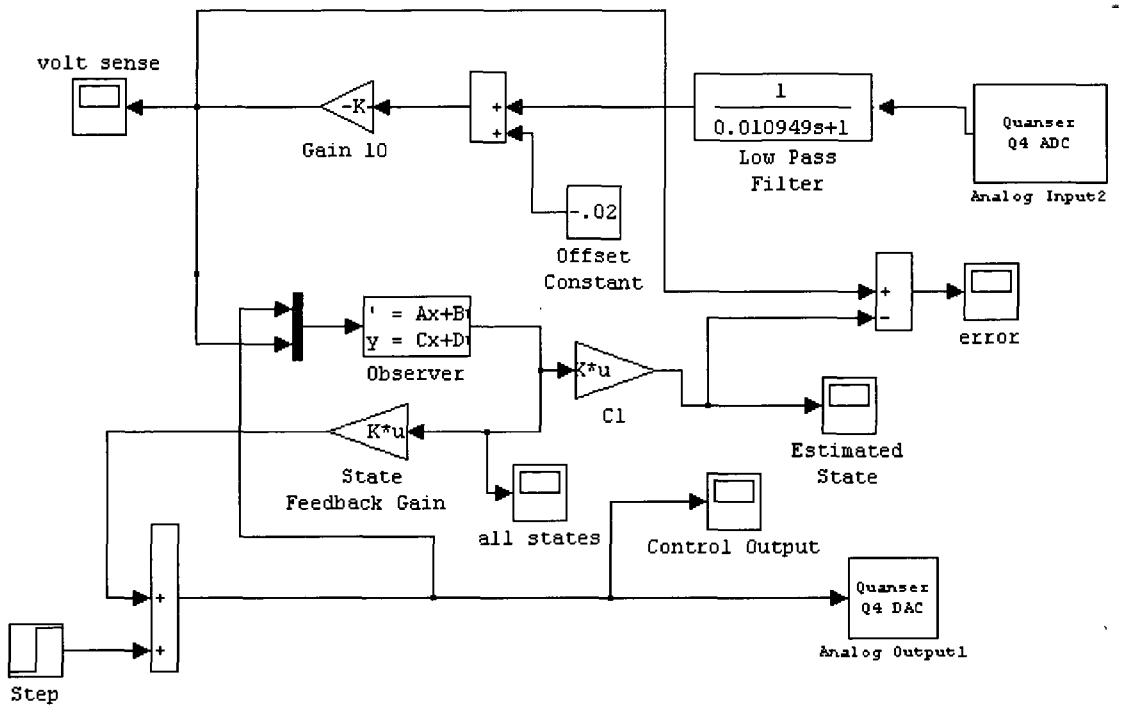

Figure 43. Real-Time Control of LQR Controller with Observer and State Feedback in Simulink.

The plots in Figure 44-48 show the vibration response with real-time control implementation of the LQR controller. Note that the settling time in real-time control is calculated using Equation (27a). For the real-time LQR control, the best control performance is shown in Figure 47 with a settling time of 1.8s, where $\alpha = 100$ and $\beta = 1$. The control voltage calculated by Simulink is about 100V, but the feasible maximum control voltage is limited to ±36V. The control voltage in Figures 46 and 48 is the calculated voltage before the ±36V cutoff of the hardware.

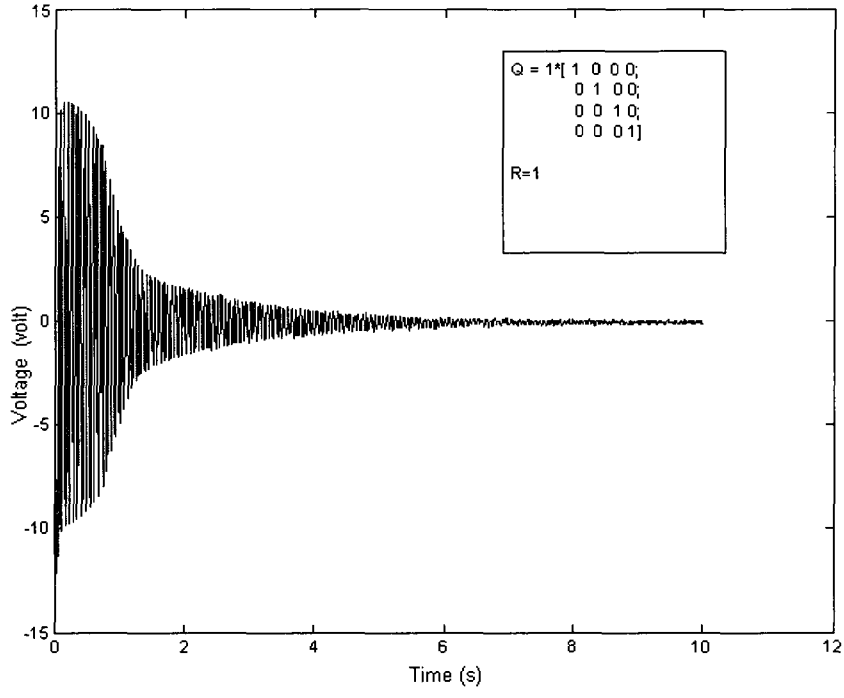

Figure 44. Real-Time Voltage Sense Plot of LQR Control at α=1, β=1.

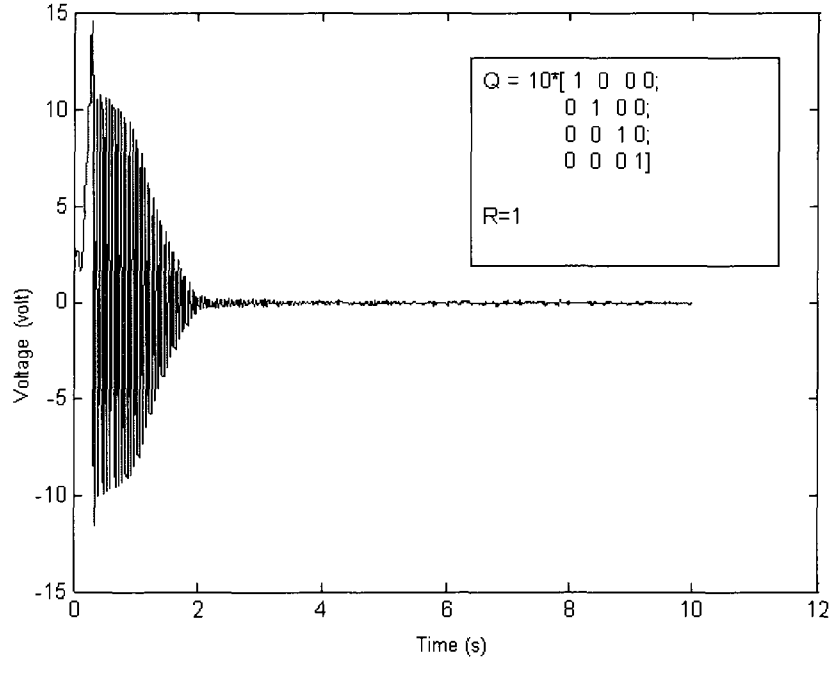

Figure 45. Real-Time Voltage Sense Plot of LQR Control at α=10, β=1.

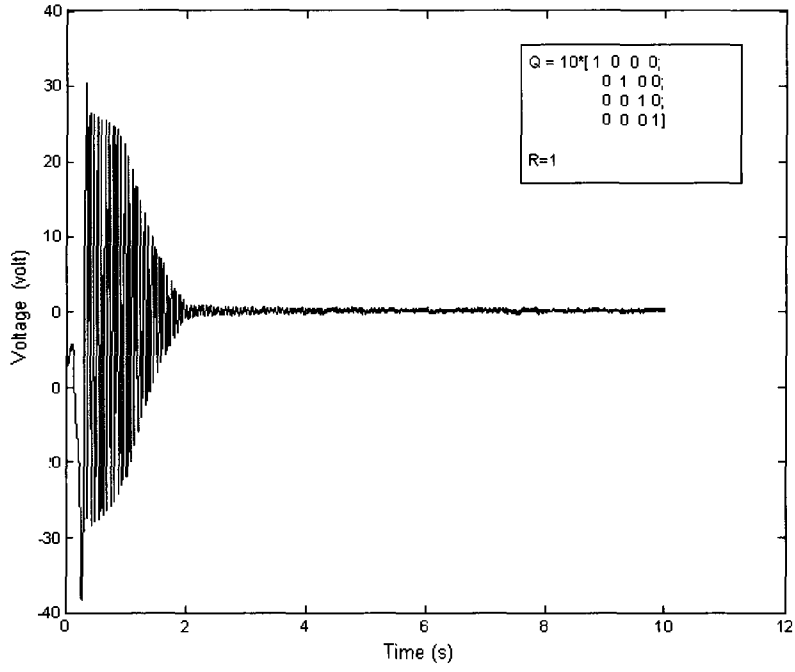

Figure 46. Real-Time Control Voltage of LQR Controller at α=10, β=1.

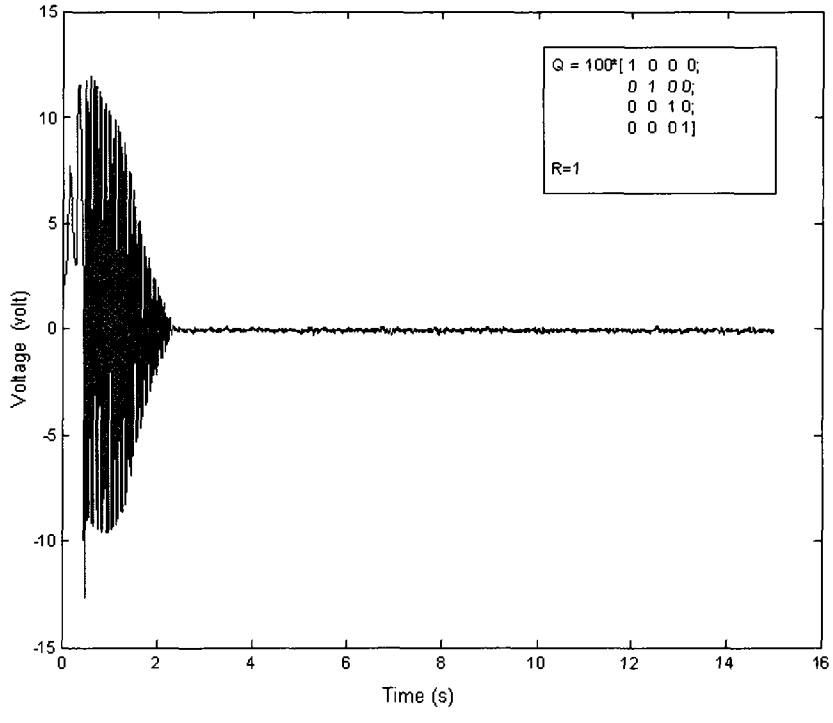

Figure 47. Real-Time Voltage Sense Plot LQR Control at α=100, β=1.

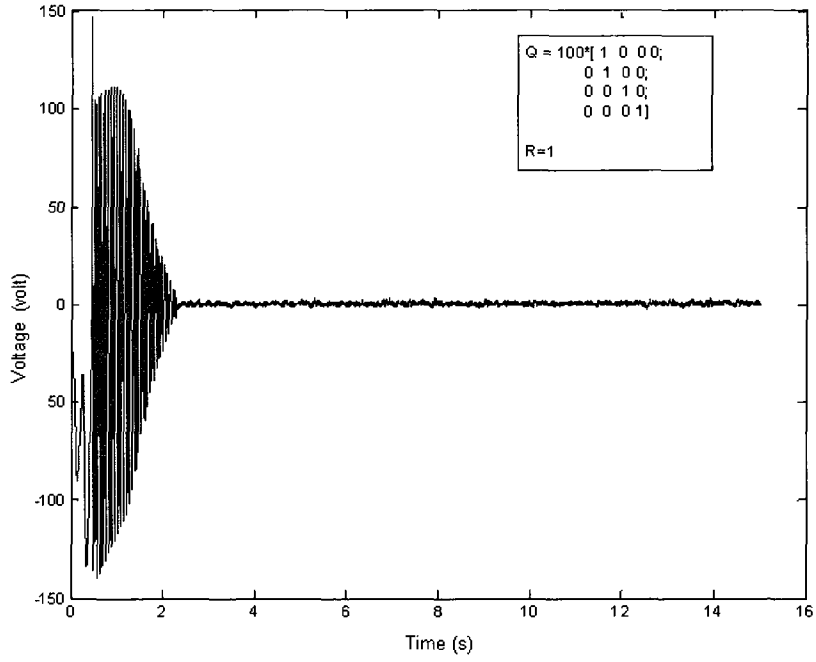

Figure 48. Real-Time Control Voltage of LQR Controller at α=100, β=1. This data shows the control voltage before the ±36V limitation of the hardware.

5. Results and Discussion

Table 5 summarizes the performance results of the open loop and close loop response with different controllers. It indicates that the LQR controller with $\alpha = 100$ and $\beta = 1$ provided the best vibration suppression with a settling time of 0.5s. As mentioned in Section 4.1, the classical control method such as the derivative control from [6] provided good damping in the first 1.5s. However, there was a small sustaining vibration that was not quickly suppressed after 1.5s. This resulted in a longer settling time of 2.5s. PD real-time control also provided a fast settling time of 1.75s. In this study, both classical control and modern control theory were successfully applied for vibration suppression of the smart structure.

The PD simulation controller 4 and real-time PD controller 5 in Table 5 have the same P and D gain, but the real-time PD gain provides better settling time performance. Thus a more aggressive controller gain, such as P = 40 and D = 1.5, is needed for faster settling time response.

Table 5. Comparison Controller Performance Based on Settling Time.

	Note: Real-time settling time calculated using Equation (27a).			
	Control Method	Control Parameters	Settling Time Response (s)	Control Voltage (V)
1	Open Loop (Real-Time)		8.75	
2	Open Loop (Simulation)		10	
3	D (*Make*)		2.5	
4	PD (Simulation)	P = 40 D=1.5	1	
5	PD (Simulation)	P = 17 D=0.01	< 6	
6	PD (Real-Time)	P = 17 D=0.01	2.25	
7	LQR (Simulation)	$\alpha = 10$ $\beta = 1$	3.5	
8	LQR (Simulation)	$\alpha = 1$ $\beta = 0.005$	1	
9	LQR (Simulation)	$\alpha = 100$ $\beta = 1$	1.2	
10	LQR (Simulation)	$\alpha = 1$ $\beta = 0.001$	0.75	
11	LQR (Real-Time)	$\alpha = 1$ $\beta = 1$	7.5	
12	LQR (Real-Time)	$\alpha = 10$ $\beta = 1$	2.5	25 max
13	LQR (Real-Time)	$\alpha = 100$ $\beta = 1$	0.5	12 max

6. Conclusion and Recommendations

First a dynamic model of a flexible beam was investigated in this thesis. The derived model obtained was based on the mode shapes, natural frequencies of the beam vibration, and the experimental damping parameter of the flexible beam. The response of the analytical beam model did not exactly fit with that of the experimental model of the beam. However, the model parameters were adjusted to match closely to the experimental data. The adjusted model provided a good understanding of the vibration of the beam. The damping coefficient for the 2^{nd} and 3^{rd} mode vibration was best estimated from the open loop response data. Because of the limitation of the hardware sampling rate, the experimental frequency response of the system was not obtained. Therefore the damping coefficient parameters also could not be obtained.

In future work, a frequency response experiment should be conducted to obtain a closer fit of the analytical model to the experimental data. Having a closer fit model, a more accurate and realistic controllers can be designed.

Other control approaches such as the H_∞ controller [8] and the sliding mode method [10] could also be implemented. The sliding mode has distinct advantages over the conventional PD approach. The sliding mode method provides robustness, and improves transient response and control accuracy [10]. This sliding method is worth studying because of its applicability in wind and seismic structure control.

In this study, the LQR state feedback method provided the best vibration suppression compared to the derivative control and PD control. Vibration suppression could be better improved by changing the Q and R weighting matrices. For future work, the maximum output voltage of the operational amplifiers powering the PZT actuators can be upgraded from ±36V to ±90V. Doing so will increase the vibration suppression effectiveness.

BIBLIOGRAPHY

[1] G. L. C. Abreu, and J. Ribeiro, "Spatial H∞ Control of a Flexible Beam Containing Piezoelectric Sensors and Actuator," University of Uberlandia, Brazil: 2004.

[2] P. Akella, " Modeling, Analysis, and Control of Flexible and Smart Structure," Michigan: UMI, 1997.

[3] T. Bailey, and E. J. Hubbard, "Distributed Piezoelectric Polymer Active Vibration Control of a Cantilever Beam," Journal of Guidance, Control, and Dynamics, vol. 8, no. 5, pp. 605-611, 1985.

[4] S. Chow, Application of Piezo Film for Active Dampening of a Cantilever Beam, Master's Thesis ed. , San Jose State University: 1993.

[5] J. Fei, "Active Vibration Control of Flexible Steel Cantilever Beam Using Piezoelectric Actuators," Proceedings of the Thirty-Seventh Southeastern, Tuskegee University, Tuskegee, Alabama: 2004.

[6] S. Griffin, "Smart Structure," Make: Technology in Your Time, vol. 13, pp. 135-141, 2008.

[7] K. Ogata, Modern Control Engineering , 4th ed. , Upper Saddle River, NJ: Prentice Hall, 2002.

[8] H. R. Pota, S. O. R. Moheimani and M. Smith, "Resonant Controller for Smart Structure," Smart Material Structure, vol. 11, pp. 1, 2002.

[9] A. Preumont, Vibration Control of Active Structure, 2nd ed., New Jersey: Kluwer Academic Publishers, 2002.

[10] G. Song, and H. Gu, " Active Vibration Suppression of a Smart Flexible Beam Using a Sliding Mode Base Controller," Journal of Vibration and Control, vol. 13, no. 8, pp. 1095-1107, 2007.

Appendix A Mathcad Analysis

Active Vibration Control of a Flexible Beam

1. Beam Dimension and Properties for Aluminum 6061

$l := 11.8in$

Length of the beam

$t := .065in$

Thickness

$w := .6in$

Width

$\rho := .0975 \frac{lbf}{in^3}$

Density

$E := 1.0878 \cdot 10^7 \frac{lbf}{in^2}$

Young Modulus

$h := \frac{t}{2}$

$wz := .0285m$

$Lz := 0.0765m$

$\rho z := 7650 \frac{kg}{m^3}$

$a := t \cdot w$

$a = 0.039\,in^2$

Cross sectional Area

$$Az := wz \cdot Lz$$

$$I := t \cdot \frac{w^3}{3}$$

$$I = 4.68 \times 10^{-3}\,in^4$$

Moment of Inertia

$$tz := .0005m$$

$$Iz := 2 \cdot \left(\frac{tz^3}{3} + t \cdot \frac{tz^2}{2} + t^2 \cdot \frac{tz}{4} \right)$$

2. Composite Material constant

$$d31 := -190 \cdot 10^{-12} \frac{m}{volt}$$

$$d31 = -7.48 \times 10^{-9} \frac{in}{volt}$$

Electric Charge Constant

$$ha := .0105in$$

Length of actuator

$$la := 1in$$

Length of sensor

$$ls := .5in$$

Thickness of PZT actuator

$$Ea := 6.6 \cdot 10^{10} \frac{N}{m^2}$$

$$Ea = 9.572 \times 10^{6}\,psi$$

Young Modulus

$ba := .4in$

width of actuator

$$d31 = -7.48 \times 10^{-9} \frac{in}{volt}$$

$$Ca := \frac{Ea \cdot d31 \cdot ba \cdot (t + ha)}{2}$$

$$Ca = -1.222 \times 10^{-4} C$$

$$Cacheck := \frac{Ea}{2} \cdot ba \cdot (t + ha)$$

$$Cacheck = 1.445 \times 10^{5} lbf$$

$$Ca = -1.081 \times 10^{-3} lbf \cdot \frac{in}{volt}$$

C is lbf*in/volt

$$Cacheck1 := Cacheck \cdot -7.48 \cdot 10^{-9} \frac{in}{volt}$$

$$1.445 \times 10^{5} lbf \cdot -7.48 \cdot 10^{-9} \frac{in}{volt} = -1.221 \times 10^{-4} C$$

$Va := 100V$

$Max := 2Ca \cdot Va$

$Max = -0.018 lbf \cdot ft$

$k31 := 0.35$

Electromagnetic coupling constant

$$g31 := -11.6 \cdot 10^{-3} \cdot \frac{m^2}{C}$$

$$g31 = -2.031 volt \cdot \frac{in}{lbf}$$

$$g31 = -17.98\,\frac{in^2}{C}$$

Mode Shape of Beam

$Az := wz \cdot Lz$

$\lambda 1 := 1.875104069$

$$Eb := 75 \cdot 10^{10}\,\frac{N}{m^2}$$

$\lambda 2 := 4.694091133$

$\lambda 3 := 7.85475743$

$c1 := .292$

$c2 := .292$

$c3 := .292$

Mode Shape 1

$t = 0.065\,in$

$$\phi 1(x) := c1 \cdot \left[\cos\left(\lambda 1 \cdot \frac{x}{1}\right) - \cosh\left(\lambda 1 \cdot \frac{x}{1}\right) - \frac{\cos(\lambda 1) + \cosh(\lambda 1)}{\sin(\lambda 1) + \sinh(\lambda 1)} \cdot \left(\sin\left(\lambda 1 \cdot \frac{x}{1}\right) - \sinh\left(\lambda 1 \cdot \frac{x}{1}\right) \right) \right]$$

$h = 8.255 \times 10^{-4}\,m$

$\phi 1(1) = -0.584$

$$\int_0^1 \phi 1(x)^2\,dx = 1.006\,in$$

Mode Shape 2

$$\phi 2(x) := c2 \cdot \left[\cos\left(\lambda 2 \cdot \frac{x}{1}\right) - \cosh\left(\lambda 2 \cdot \frac{x}{1}\right) - \frac{\cos(\lambda 2) + \cosh(\lambda 2)}{\sin(\lambda 2) + \sinh(\lambda 2)} \cdot \left(\sin\left(\lambda 2 \cdot \frac{x}{1}\right) - \sinh\left(\lambda 2 \cdot \frac{x}{1}\right) \right) \right]$$

$\phi 2(l) = 0.584$

$$\int_0^l \phi 2(x)^2 \, dx = 1.006\,in$$

Mode Shape 3

$$\phi 3(x) := c3 \cdot \left[\cos\left(\lambda 3 \cdot \frac{x}{l}\right) - \cosh\left(\lambda 3 \cdot \frac{x}{l}\right) - \frac{\cos(\lambda 3) + \cosh(\lambda 3)}{\sin(\lambda 3) + \sinh(\lambda 3)} \cdot \left(\sin\left(\lambda 3 \cdot \frac{x}{l}\right) - \sinh\left(\lambda 3 \cdot \frac{x}{l}\right) \right) \right]$$

$\phi 3(11.8in) = -0.584$

$$\int_0^l \phi 3(x)^2 \, dx = 1.006\,in$$

Natural Frequency of the first 3 modes

$$\beta 1 := \frac{\lambda 1}{l}$$

$$\beta 1 = 1.907 \, \frac{1}{ft}$$

$$\Omega 1 := \int_0^l \phi 1(x) \cdot \frac{d^4}{dx^4} \phi 1(x) \, dx$$

$$\Omega 1 = 6.415 \times 10^{-4} \, \frac{1}{in^3}$$

$$\beta 2 := \frac{\lambda 2}{l}$$

$$\beta 2 = 4.774 \, \frac{1}{ft}$$

$$\beta 3 := \frac{\lambda 3}{l}$$

$$\beta 3 = 7.988 \frac{1}{ft}$$

$$\Omega 2 := \int_0^1 \phi 2(x) \cdot \frac{d^4}{dx^4} \phi 2(x)\, dx$$

$$\Omega 2 = 0.025 \frac{1}{in^3}$$

$$\Omega 3 := \int_0^1 \phi 3(x) \cdot \frac{d^4}{dx^4} \phi 3(x)\, dx$$

$$\Omega 3 = 0.198 \frac{1}{in^3}$$

$$w1 := \left(\frac{E \cdot I \cdot \Omega 1}{\rho \cdot a} \right)^{\frac{1}{2}}$$

$$w1 = 92.677\, rad$$

$$I = 2.257 \times 10^{-7}\, ft^4$$

$$wcheck := \frac{E \cdot I \cdot \beta 1^4}{\rho \cdot a}$$

$$wcheck = 1.024 \times 10^5 \frac{1}{ft}$$

$$w2 := \left(\frac{E \cdot I \cdot \Omega 2}{\rho \cdot a} \right)^{\frac{1}{2}}$$

$$w2 = 580.799\, rad$$

$$w3 := \left(\frac{E \cdot I \cdot \Omega 3}{\rho \cdot a}\right)^{\frac{1}{2}}$$

$$w3 = 1.626 \times 10^{3}\ \text{rad}$$

$$\frac{w(x,s)}{Va(s)} = \sum_{i} \frac{\left(k_a \cdot \phi(x)\right) \cdot \left(\phi i(xa2)' - \phi i(xa1)'\right)}{s^2 + 2\zeta_i \cdot W_{ni} \cdot s + \left(W_{ni}\right)^2}$$

$$Ca = -1.222 \times 10^{-4}\ C$$

$$ka := \frac{Ca}{\rho \cdot a}$$

NOTE: A is ampere

$$ka = -8.321 \times 10^{-5}\ \frac{s^3 \cdot A}{lb}$$

$$\rho \cdot a = 1.468\ \frac{lb}{s^2}$$

$$\frac{Vs(s)}{Va(s)} = \sum_{i} \frac{\left[\left(k_s \cdot k_a\right) \cdot \phi(x)\right] \cdot \left(\phi i(xs2)' - \phi i(xs1)'\right) \cdot \left(\phi i(xa2)' - \phi i(xa1)'\right)}{s^2 + 2\zeta_i \cdot W_{ni} \cdot s + \left(W_{ni}\right)^2}$$

$$ka = -9.985 \times 10^{-4}\ \frac{s^2}{ft} \cdot C \cdot \frac{in}{lb}$$

Location of Actuator

Position of Actuator

$$xa1 := 0in$$

Position of Actuator

$$xa2 := xa1 + la$$

$xa2 = l\ in$

Find the numerator of the Laplace transform of the system describing the beam tip deflection

input.

$kd := l$

$num1b := kd \cdot \phi1(l)$

$num1b = -0.584$

$num2b := kd \cdot \phi2(l)$

$num2b = 0.584$

$num3b := kd \cdot \phi3(l)$

$num2b = 0.584$

$num1b + num2b + num3b = -0.584$

$$ka = -8.321 \times 10^{-5}\ \frac{s^3 \cdot A}{lb}$$

Find the numerator of the Laplace transform of the system describing the elastic deflection

of the flexible beam due to a voltage applied by actuating the piezoelectric.

The Laplace transform of Vs(s)/Va(s). The is the relation between

the voltage applied to the actuator and the voltage induced in the piezoelectric sensor.

$$num1 := \left[\left(\frac{d}{dxa2}\phi1(xa2)\right) - \left(\frac{d}{dxa1}\phi1(xa1)\right)\right] \cdot ka \cdot \phi1(l)$$

$bs := ba$

Width of the sensor is equal to width of the actuator

$$num1 = -8.098 \times 10^{-6} \frac{s^3 \cdot A}{lb \cdot ft}$$

$hs := ha$

Thickness of the sensor is equal to the width of the actuator.

$t = 0.065\,in$

$$ks := -bs \cdot \left(hs + \frac{t}{2}\right) \cdot \frac{k31^2}{g31}$$

$ks = 1.172 \times 10^{-4}\,C$

(Gustavo)

$$num2 := \left[\left(\frac{d}{dxa2}\phi 2(xa2)\right) - \left(\frac{d}{dxa1}\phi 2(xa1)\right)\right] \cdot ka \cdot \phi 2(l)$$

$$num2 = 4.299 \times 10^{-5} \frac{s^3 \cdot A}{lb \cdot ft}$$

$xs1 := xa2 + 0.5in$

$xs1 = 1.5\,in$

Location of the sensor base

$xs2 := xs1 + ls$

$xs2 = 2\,in$

Location of sensor end

$$num3 := \left[\left(\frac{d}{dxa2}\phi 3(xa2)\right) - \left(\frac{d}{dxa1}\phi 3(xa1)\right)\right] \cdot ka \cdot \phi 2(l)$$

$$num3 = 1.009 \times 10^{-4} \frac{s^3 \cdot A}{lb \cdot ft}$$

$ks = 1.172 \times 10^{-4}\,C$

Find the denominator of the transfer function

$$nums1 := \left[\left(\frac{d}{dxs2}\phi 1(xs2)\right) - \left(\frac{d}{dxs1}\phi 1(xs1)\right)\right]\cdot ks$$

Numerator of TF for sensor 1

$\zeta 1 := .007$

Damping Coefficient for mode 1

Damping Coefficient for mode 2

$$nums1 = -8.255 \times 10^{-6}\ \frac{s\cdot A}{ft}$$

$$nums1 = -6.879 \times 10^{-7}\ \frac{C}{in}$$

$\zeta 2 := .007$

Damping Coefficient for mode 3

$\zeta 3 := .007$

$$nums2 := \left[\left(\frac{d}{dxs2}\phi 2(xs2)\right) - \left(\frac{d}{dxs1}\phi 2(xs1)\right)\right]\cdot ks$$

$2\cdot\zeta 1\cdot w1 = 1.297$

w1 is the natural frequency for mode 1

$w1 = 92.677$

$w1^2 = 8.589 \times 10^3$

$$nums2 = -1.947 \times 10^{-5}\ \frac{s\cdot A}{ft}$$

$$nums2 = -1.623 \times 10^{-6}\ \frac{C}{in}$$

$2\cdot\zeta 2\cdot w2 = 8.131$

w2 is the natural frequency for mode 2

$$w2^2 = 3.373 \times 10^5$$

$$nums3 := \left[\left(\frac{d}{dxs2}\phi 3(xs2)\right) - \left(\frac{d}{dxs1}\phi 3(xs1)\right)\right]\cdot ks$$

$$w2 = 580.799$$

$$2\cdot\zeta 3\cdot w3 = 22.768$$

$$nums3 = 1.876 \times 10^{-5}\ \frac{s\cdot A}{ft}$$

$$nums3 = 1.564 \times 10^{-6}\ \frac{C}{in}$$

w3 is the natural frequency for mode 3

$$w3^2 = 2.645 \times 10^6$$

For calculation of state space use for m file

$$\frac{w(x,s)}{Va(s)} = \sum_i \frac{\left(k_a\cdot\phi(x)\right)\cdot\left(\phi i(xa2) - \phi i(xa1)\right)}{s^2 + 2\zeta_i\cdot W_{ni}\cdot s + \left(W_{ni}\right)^2}$$

$$nums1ss := \left[\left(\frac{d}{dxs2}\phi 1(xs2)\right) - \left(\frac{d}{dxs1}\phi 1(xs1)\right)\right]\cdot ks\cdot\phi 1(1)$$

$$nums2ss := \left[\left(\frac{d}{dxs2}\phi 2(xs2)\right) - \left(\frac{d}{dxs1}\phi 2(xs1)\right)\right]\cdot ks\cdot\phi 1(1)$$

$$\left(\frac{num1}{s^2 + 2\cdot\zeta 1\cdot w1 + w1^2} + \frac{num2}{s^2 + 2\cdot\zeta 2\cdot w2 + w2^2} + \frac{num3}{s^2 + 2\cdot\zeta 3\cdot w3 + w3^2}\right)$$

$$nums3ss := \left[\left(\frac{d}{dxs2}\phi 3(xs2)\right) - \left(\frac{d}{dxs1}\phi 3(xs1)\right)\right]\cdot ks\cdot\phi 1(1)$$

$$nums1ss = 4.821 \times 10^{-6}\ \frac{s\cdot A}{ft}$$

$$nums2ss = 1.137 \times 10^{-5} \frac{s \cdot A}{ft}$$

The Transfer function for mode 1,2, and 3 respectively calculated from Matlab

$$nums3ss = -1.096 \times 10^{-5} \frac{s \cdot A}{ft}$$

for State Space B matrix

$$phi1 := \left[\left(\frac{d}{dxa2}\phi 1(xa2)\right) - \left(\frac{d}{dxa1}\phi 1(xa1)\right)\right]$$

$$phi1 = -0.014 \frac{1}{in}$$

$$phi2 := \left[\left(\frac{d}{dxa2}\phi 2(xa2)\right) - \left(\frac{d}{dxa1}\phi 2(xa1)\right)\right]$$

$$phi2 = -0.074 \frac{1}{in}$$

$$phi3 := \left[\left(\frac{d}{dxa2}\phi 3(xa2)\right) - \left(\frac{d}{dxa1}\phi 3(xa1)\right)\right]$$

$$phi3 = -0.173 \frac{1}{in}$$

for State space C matrix

$$phi1xs := \left[\left(\frac{d}{dxs2}\phi 1(xs2)\right) - \left(\frac{d}{dxs1}\phi 1(xs1)\right)\right]$$

$$phi1xs = -5.87 \times 10^{-3} \frac{1}{in}$$

Combine the numerator for the sensor and actutator to find the overall numerator of the transfer

function.

$$phi2xs := \left[\left(\frac{d}{dxs2}\phi 2(xs2)\right) - \left(\frac{d}{dxs1}\phi 2(xs1)\right)\right]$$

$$phi2xs = -0.014\,\frac{1}{in}$$

$$Num1overall := \frac{num1 \cdot nums1}{\phi 1(1)}$$

$$Num1overall = -2.716 \times 10^{-9}\ F$$

$$phi3xs := \left[\left(\frac{d}{dxs2}\phi 3(xs2)\right) - \left(\frac{d}{dxs1}\phi 3(xs1)\right)\right]$$

$$phi3xs = 0.013\,\frac{1}{in}$$

$$Num2overall := \frac{num2 \cdot nums2}{\phi 2(1)}$$

$$Num2overall = -3.402 \times 10^{-8}\ F$$

phi1pxs

$$Num3overall := \frac{num3 \cdot nums3}{\phi 3(1)}$$

$$Num1overall = -2.716 \times 10^{-9}\ F$$

phi2pxs

$$Num1overall = -9.539 \times 10^{-12}\ \frac{s^2}{ft}\ s^2 \cdot \frac{A^2}{lb \cdot in}$$

$$phi1xa := \left(\frac{d}{dxa2}\phi 1(xa2)\right) - \left(\frac{d}{dxa1}\phi 1(xa1)\right)$$

$$phi1xa = -0.014\,\frac{1}{in}$$

$$phi2xa := \left(\frac{d}{dxa2}\phi 2(xa2)\right) - \left(\frac{d}{dxa1}\phi 2(xa1)\right)$$

$$\text{phi2xa} = -0.074 \frac{1}{\text{in}}$$

$$\text{phi3xa} := \left(\frac{d}{dxa2}\phi 3(xa2)\right) - \left(\frac{d}{dxa1}\phi 3(xa1)\right)$$

$$\text{phi3xa} = -0.173 \frac{1}{\text{in}}$$

Appendix B Matlab M Files

```
%Properties of Aluminum 6061
l=11.8;    %in  length of beam
t=0.05;    %in  thickness of beam
w=0.6;     %in  width of beam
ro=0.0975; %lb/in^3
E = 1.0878E7; %lb/in^2
a=t*w;     %in^2
I=t*w^3/3  %Moment of Inertia

%Properties of PZT
d31=-7.48E-9  %in/volt
ha=.0105     %in height of actuator
hs=ha;       %in height of sensor
la=1         %in, length of actuator
ls=.5        %in, length of sensor
Ea=9.572E6   %lb/in^2
ba=.4        %in,  width of actuator
bs=ba        %in,  width of sensor
Cs=.008E-6;  %capacitance per unit area
xs1=3.8;     %location of sensor
xs2=4.3;     %location of sensor
Ca=Ea*d31*ba*(t+ha)/2; %lb*in/volt Geometry coefficient
```

```
Ca=2*Ca      %two collocated actuator

k31=.35;     %coupling coefficient

g31=(-11.6E-3)*(39.368)^2  %in^2/C

omega1=6.415E-4;  % 1/in^3

omega2=0.025;     %1/in^3

omega3=0.198;     %1/in^3


w1=(E*I*omega1/(ro*a))^.5;    %1st natural freq rad

w2=(E*I*omega2/(ro*a))^.5;    %2nd natural freq rad

w3=(E*I*omega3/(ro*a))^.5;    %3rd natural freq rad

w1a=97.5;

w2a=589.5;

z1=0.0052;  %damping coefficient

z2=0.001;

z3=0.001;


%actuator and sensor constant

ka=Ca/(ro*a)  % in^2/volt

ks=-bs*(hs+t/2)*(k31^2/g31)  %Coulomb or can be in*lb/volt


phi1xa=-0.014;  %derivative of mode shape 1 of actuator at location 2 - location 1

phi2xa=-.074;   %derivative of mode shape 2 of actuator at location 2 -        location 1
```

```
phi3xa=-.173;  %derivative of mode shape 3 of actuator at location 2 - location 1
phi1xs=-5.87E-3;  %derivative of mode shape 1 of sensor at location 2 - location 1
phi2xs=-0.014;     %derivative of mode shape 2 of sensor at location 2 - location 1
phi3xs=.013;       %derivative of mode shape 3 of sensor at location 2 - location 1

%Transfer function of Vs/Va
nums1=ks*ka*phi1xs*phi1xa/(Cs*bs*(xs2-xs1)); %numerator of transfer funciton, first
mode
nums2=ks*ka*phi2xs*phi2xa/(Cs*bs*(xs2-xs1));
nums3=ks*ka*phi3xs*phi3xa/(Cs*bs*(xs2-xs1));
den1=[1 2*z1*w1a w1a^2]; %denominator of transfer function, first mode
den2=[1 2*z2*w2a w2a^2]; %denominator of transfer function, 2nd mode
den3=[1 2*z3*w3 w3^2]; %denominator of transfer function, 2nd mode
tf_mode1=tf(nums1,den1); %transfer function of first mode.
tf_mode2=tf(nums2,den2);
tf_mode3=tf(nums3,den3);
t=0:.01:5;
Tf_mode=tf_mode1+tf_mode2+0; % add the transfer for first 3 mode
[numoverall,denoverall] = TFDATA(Tf_mode,'v')
damp(conv(conv(den1,den2),den3));
```

```
%calculate state space
A1=[0 1 0 0;
  -w1^2 -(w1)*2*z1 0 0;
  0 0 0 1;
  0 0 -w2^2 -(w2)*2*z2];
B1=ka*[phi1xa 0 phi2xa 0]';
C1=(ks/(Cs*bs*(xs2-xs1)))*[phi1xs 0 phi2xs 0];
D1=[0];
D2=[0 0 0 0]';
%step(A1,B1,C1,D1)
p=[-100+j*100 -100-j*100 -500+j*2000 -500-j*2000]
pc=.1*p
k1=place(A1,B1,pc)
%Bode(A1,B1,C1,D1);grid;
AC=A1-B1*k1;
%step(A1,B1,C1,D1)
%step(AC,B1,C1,D1)
C2=[1 0 0 0;
   0 1 0 0;
   0 0 1 0;
   0 0 0 1];
```

```
po=[-1+1i -1-1i -5+2i -5-2i]';
pob=1*po
ke=place(A1',C1',po);
ke=ke'
Aob=A1-ke*C1;
Bob=[B1 ke]

%Controllability and Observability
co=ctrb(A1,B1)
ob=obsv(A1,C1)
observability=rank(co)
controllability=rank(ob)

%lqr
Q=1*[10 0 0 0;
   0 1 0 0;
   0 0 10 0;
   0 0 0 1];
R=.001;  %R=.001 works
[ke2,S,E]=lqr(A1,B1,Q,R);
```